

Accepted for publication in *the Astrophysical Journal* and it is scheduled for ApJ February 20, 2007, v 656, 2 issue

Effects of Downscattering on the Continuum and Line Spectra in Powerful Wind Environment. Monte Carlo Simulations, Analytical Results and Data Analysis

Philippe Laurent^{1,2} and Lev Titarchuk^{3,4}

ABSTRACT

In Paper by Titarchuk & Shrader the general formulation and results for photon reprocessing (downscattering) that included recoil and Comptonization effects due to divergence of the flow were presented. Here we show the Monte Carlo (MC) simulated continuum and line spectra. We also provide an analytical description of the simulated continuum spectra using the diffusion approximation. We have simulated the propagation of monochromatic and continuum photons in a bulk outflow from a compact object. Electron scattering of the photons within the expanding flow leads to a decrease of their energy which is of first order in V/c (where V is the outflow velocity). The downscattering effect of first order in V/c in the diverging flow is explained by semi-analytical calculations and confirmed by MC simulations. We conclude that redshifted lines and downscattering bumps are intrinsic properties of the powerful outflows for which Thomson optical depth is greater than one. We fitted our model line profiles to the observations using four free parameters, $\beta = V/c$, optical depth of the wind τ , the wind temperature kT_e and the original line photon energy E_0 . We show how the primary spectrum emitted close to the black hole is modified by reprocessing in the warm wind. In the framework of the our wind model the fluorescent iron line K_α is formed in the partly ionized wind as a result of illumination by central source continuum photons. The demonstrated application of our outflow model

¹CEA/DSM/DAPNIA/SAP, CEA Saclay, 91191 Gif sur Yvette, France; Fédération APC, Collège de France, 75231 Paris, France; plaurent@cea.fr

²Fédération APC, Collège de France, 75231 Paris, France

³George Mason University/Center for Earth Observing and Space Research, Fairfax, VA 22030; and US Naval Research Laboratory, Code 7655, Washington, DC 20375-5352; ltitarchuk@ssd5.nrl.navy.mil

⁴NASA/ Goddard Space Flight Center, code 660, Greenbelt MD 20771, lev@lheapop.gsfc.nasa.gov

to the XMM observations of MCG 6-30-15, and to the ASCA observations of GRO J1655-40, points out a potential powerful spectral diagnostic for probes of the outflow-central object connection in Galactic and extragalactic BH sources.

Subject headings: accretion—stars: radiation mechanisms: nonthermal

1. Introduction

Titarchuk & Shrader (2005), Paper I, hereafter TSh05, have shown that downscattering modification of the primary photon spectrum by an outflowing plasma is a possible mechanism for producing the continuum excess in the ~ 10 keV spectral region. This continuum excess can be formed only if the energy index of the primary photon spectrum is less than one (see also Sunyaev & Titarchuk 1980, hereafter ST80). This is usually attributed to Comptonization by a static reflector, such as a downward- or obliquely-illuminated accretion disk, although the overall continuum form differs from that of the basic Compton reflection form. TSh05 thus suggest, that in at least some cases, the outflow downscattering effect rather than the standard Compton reflection mechanism is responsible for the observed "excess" hard-X-ray continuum.

To obtain a description of the X-ray photon spectrum, many authors (see e.g. Gilfanov, Churazov & Revnivtsev 1999, hereafter GCR99, Pottschmidt et al. 2003, and etc) used an empirical model in which each source spectrum is a sum of power law spectrum with photon index Γ and a multi-temperature disk blackbody. To this continuum, a reflection spectrum after Magdziarz & Zdziarski (1995) was added. However, Shaposhnikov & Titarchuk (2006), hereafter ST06 argue that these spectral features are results of reprocessing of the central source hard radiation in the outflow (warm wind) that surrounds the central BH. This claim is supported by observed power decay of quasiperiodic oscillations (QPOs) towards the softer states that is presumably a result of reprocessing of time signal in the extended relatively warm wind (see Fig. 6 in ST06).

The basic idea is that electron scattering of photons from a central source entering the expanding outflow experience a decrease in energy (downscattering). The magnitude of this decrease is of first order in V/c and in $E/m_e c^2$ where V is the outflow speed, c is the speed of light, E is the initial photon energy and m_e is the electron rest mass.

TSh05 have developed an analytic formulation for the emergent spectrum resulting from photon diffusion in a spherically expanding Comptonizing media, characterized by two model parameters: an average number of scatterings in the medium N_{av} , and efficiency the energy loss in the divergent flow ε . In this formulation of the Radiative Transfer problem,

the number of photons emitted in the wind shell equals that which escape to the Earth observer (i.e. the photon number is conserved). Consequently, if the high energy photons lose their energy on the way out but the number of photons is conserved, it has to result in the accumulation of the photons at a particular lower energy band.

The basic idea of the wind photon downscattering is depicted in Figure 1. There presents a simple explanation of the diverging flow effect on the photon propagation through the medium. A photon emitted outwards near inner boundary and then scattered at a certain point by an electron moving with velocity \mathbf{V}_1 , is received by an electron moving with velocity \mathbf{V}_2 as shown with frequency $\nu_2 = \nu_1 [1 + (\mathbf{V}_1 - \mathbf{V}_2) \cdot \mathbf{n}/c]$ where \mathbf{n} is a unit vector along the path of the photon at the scattering point. In a diverging flow $(\mathbf{V}_1 - \mathbf{V}_2) \cdot \mathbf{n}/c < 0$ and photons are successively redshifted, until scattered to an observer at infinity. The color of photon path (in Figure 1) indicates the frequency shift in the rest frame of the receiver (electron or the Earth observer). On the other hand, referring to the right-hand side of Figure 1, in a converging flow $(\mathbf{V}_1 - \mathbf{V}_2) \cdot \mathbf{n}/c > 0$ and photons are blueshifted.

In this Paper we present the results of extensive Monte Carlo simulations of the downscattering effects in the wind (diverging flow). In addition to the scattering, Doppler and Compton effects we include a photoabsorption effect in the diverging flow (wind). Any photon with energy of about 7-8 keV and higher interacting with outflow plasma is more likely to be absorbed by the flow and be reemitted at energies about 6.4-6.6 keV, depending on the ionization stage of the flow (see Kallman et al. 2004). Laming and Titarchuk (2004), hereafter LT04, calculated the temperature and ionization balance in the outflow determined by seeking the temperature at which the outflowing gas attains photoionization-recombination equilibrium. The gas is heated by Compton scattering and photoionizations by photons from the central compact object and is cooled by radiation, ionization, and adiabatic expansion losses. The solution of this problem is general regarding the calculation of the temperature and ionization balance in the target illuminated by the hard radiation. It potentially has many applications beyond Astrophysics (for example, in Radiation Safety Physics). Our simulations allow us to reveal *the spectral, timing and absorption properties of the emergent radiation*.

We update the analytical results of the downscattering modifications of the continuum obtained by TSh05 (using Fokker-Planck technique) and we verify them using the Monte Carlo (MC) simulated spectra. We demonstrate that the analytical formulas for the continuum spectra well describe the MC spectra almost for any $\beta = V/c \lesssim 0.8$.

Many authors [e.g. Tanaka et al. (1995); Nandra et al. (1997); Wilms et al. (2001); Uttley et al. (2004); Miller et al. (2004a,b)] have found unusual curvature (red-skewed features) at energies between 2 and 8 keV in X-ray spectra of a number of galactic and

extragalactic BH sources. Significantly the fluxes of these features remain nearly *constant* despite the large changes in the continuum flux as shown in the observations of MCG-6-30-15, NGC 4051 and others [Markovitz, Edelson, & Vaughan (2003)]. This lack of variability means that fast changes (which are almost certain to occur near the BH) are not obtained. These observations motivate us to make a detailed study of the spectral line formation in the outflows that possibly occur in black hole sources. In this Paper we demonstrate that red-skewed features can be a result of scattering of iron line photons in the powerful outflow.

We offer a model in which the hard radiation of the central object illuminates and heats the outflow (wind) region originated in the outskirts of the disk (well outside the innermost part of the accretion disk near the BH). The line photons are generated and scattered in the outflow. Our basic scenario is illustrated in Figure 1. The wind originates at a distance r_{in} from the central black hole and is of a density such as to give a Thomson scattering optical depth τ_T close to unity far from the black hole. The optical depth in the Fe K continuum is about 1-3 times higher than that due to electron scattering (assuming a solar abundance of Fe, and depending on charge state, see Kallman et al. 2004), and so Fe $K\alpha$ formed by inner shell ionization of Fe ions in the outflow by the continuum from the central black hole only comes from a smaller inner region. In fact, using the calculations of the ionization state of the outflow shell by LT04, we find that $K\alpha$ -photon sources are exponentially distributed over a skin at the bottom of the outflow, the skin thickness being 4% of the optical depth of the wind shell. Furthermore because the iron photo-absorption opacity σ_K is about few times the Thomson opacity, σ_T , any photon around the K-absorption edge energy must be absorbed. In fact, these edges are seen with the strong $K\alpha$ lines during X-ray superbursts detected from NS source 4U 1820-30 (see Figs. 5 and 9 in Strohmayer & Brown 2002).

A thorough analysis and review of the diffusion theory of photon propagation in an optically thick fluid in bulk outflow has been provided by Titarchuk, Kazanas & Becker (2003), hereafter TKB. They show that the iron line is produced in an effectively optically thick medium. Its red wing is the result of multiple scattering, each scattering producing a first order V/c -redshift. This process produces a red wing to the line without any particular fine-tuned geometric arrangement.

The TSh05 and TBK results are obtained using the Fokker-Planck equation [Blandford & Payne (1981) see also Lifshitz & Pitaevsky (1981) for a general treatment of the particle acceleration problem] which is valid for $\beta = V/c \ll 1$ and $\tau_{eff} > 1$. The MC method does not have these limitations.

We show the results of MC simulations of scatterings of continuum and monochromatic photons for various values of plasma temperatures kT_e , outflow bulk velocity β , and Thomson optical depth τ . The details of the MC method applied to the outflow model are given in §2.

We compare the results of the MC simulated continuum with their analytical description and discuss the downscattering modifications of the incident spectrum in §§3.1-3.2. The results of the simulated line formation in the outflow and its explanation using the analytical theory are shown in §3.3. Examples of the model fits to the XMM data obtained for MCG-6-30-15 and to ASCA archive data of galactic BHs are shown in §4. The results of the simulations of overall spectra including the scattering, photon absorption effects are presented in §5. Discussion and conclusions follow in §6.

2. Details of the Monte Carlo Method

Laurent & Titarchuk (1999), hereafter LT99, simulated the Comptonization of photons using a Monte-Carlo method in the Schwarzschild metric. The geometry used in these simulations consists of a spherical shell harboring a black hole in its center. Once given the cloud Thomson optical depth τ , N_e is an electron number density measured in the local rest frame of the flow that is

$$N_e = \tau(r_S/r)^2 / [r_S \sigma_T (r_S/r_{in} - r_S/r_{out})]. \quad (1)$$

Here σ_T is the Thomson cross section, r_{in} and r_{out} are the inner and outer radii of the shell respectively, and r_S is the Schwarzschild radius. Simulations made for different values of r_{in} and r_{out} (that are much greater than the Schwarzschild radius) have shown no change of the line profile and continuum provided the shell optical depth remains the same. We have varied the shell electron temperature from 0.01 to 1 keV. Along with the thermal motion of the electrons in the cloud, we have also taken into account the bulk velocity of the outflow $\beta = V/c$. In these simulations, the spherical wind has a constant bulk velocity within the flow. It is worth noting that an increase of the shell temperature from 0.01 to 1 keV slightly increases the blue wing of the observed line, but induces no change in the red wing that we are mostly interested in here.

For the timing studies described in the next section we have also computed the path length that each photon in the simulations has covered until it escapes from the shell.

3. Downscattering effect in an outflow

The problem of photon propagation in a fluid in bulk motion has been studied in detail in a number of papers [see e.g. Blandford & Payne (1981), Payne & Blandford (1981), Nobili, Turolla & Zampieri (1993); Titarchuk, Mastichiadis & Kylafis (1997); TKB; TSh05; Laurent & Titarchuk (1999), (2001)]. In particular, TSh05 present a general formulation and

a solution of the spectral formation in the diverging outflow. They demonstrated that the resulting spectrum can be formed as a convolution of energy and spatial diffusion solutions.

To apply these Radiative Transfer results to observational data, TSh05 have developed a generic analytical formulation which leads to a simple analytic expression for modification of the emergent spectrum due to recoil and velocity divergence effects in the flow. For the recoil effect, TSh05 extend the results by Sunyaev & Titarchuk (1980), hereafter ST80, who show that the downscattering feature, or "bump", can appear superposed on power-law spectra with energy spectral indices $\alpha < 1$ as a result of photon diffusion through a static cloud. From ST80 and calculations presented in TSh05, one might conclude such bumps are not a necessarily a feature of disk reflection, but they can be also formed as a result of the photon reprocessing in a relatively cool, ambient plasma characterized by temperatures of order 10^6 K.

3.1. Time distributions of escape photons

In order to understand and explain the shapes and the main features of the MC simulated spectra we attempted to reproduce them using the analytical diffusion approximation. In framework of the diffusion theory (TSh05) the resulting spectrum can be presented as a particular convolution of a primary photon spectrum $\varphi(z)$ and a time distribution of escape photons $\mathcal{P}(u)$ (see Eq. 2, below). Here $u = t/t_{fp}$, t and $t_{fp} = l/c$ are the time for photon to escape from the wind and the mean free path time between two consequent photon scatterings respectively; $z = E/m_e c^2$ is the dimensionless photon energy. ST80 and Sunyaev & Titarchuk (1985) hereafter ST85, demonstrate that the photon escape distribution $\mathcal{P}(u)$ exponentially decays with u as $u > 1$ for any bounded configuration, namely $\mathcal{P}(u) \sim b \exp(-bu)$.

In Figure 2 we present the simulated time distribution $\mathcal{P}(t/t_{fp})$ for optical depth of the wind τ equal to 4. As it was found by ST80 and ST85, the time distribution decay exponentially $\exp(-bt/t_{fp})$ for $t > t_{fp}$ when the photons propagate in any bounded medium. This result is used for derivation of the analytical spectra (see Eqs 2). It means that the best-fit b -parameters obtained by fitting $\exp(-bt/t_{fp})$ to the time distributions and those b -parameters obtained by fitting the analytical spectra to the simulated spectra are identical within errors of b . We computed the b -values obtained by these ways and we found they are identical. This consistency check gives us more confidence of accuracy of our simulations and their analytical description.

In Figure 3 we show the photon distribution for emergent photons over a range of deflecting angles with respect of the direction of the incident photons. The outflow shell

is radially illuminated by the central source radiation. The simulations are presented for $\tau = 1, 2, 4$ and $\beta = 0.1$. In fact, we find in our simulations that the distribution of the scattering component weakly depends on τ . Practically, there is little difference between that related to $\tau = 4$, and $\tau = 1, 2$. There is only the difference in the normalization of the direct (non-scattering) component A_N for which the ratio of $A_N(\tau = 4)/A_N(\tau) = \exp(-4 + \tau)$. The distribution has a strong maximum about 50° . Thus we expect that our results for spherical wind can be applicable for the conical wind if the half-angle of the conical wind is about 50° or more (wide open jet or wind).

As we demonstrate in Figure 2 the simulated escape time distribution in the wind has an exponential profile which is a typical signature of the photon diffusion propagation in any bounded configuration (ST85). This leads us to conclusion that we can also treat the radiative transfer in the wind in the framework of the diffusion model (see TSh05).

3.2. Monte Carlo simulated spectra of the continuum and their analytical description

For the completeness of the present work we reproduce some necessary details of the analytical diffusion model by TSh05. Particularly, the downscattering modification of the incident spectrum $\varphi(E)$ can be obtained using formula (24) in TSh05:

$$\mathcal{F}_\nu(z, \varepsilon) = \frac{1}{z} \int_0^{u_{max,\varepsilon}(z)} e^{-4\varepsilon u/3} \psi^{(\varepsilon)}(z, u) \varphi[\psi^{(\varepsilon)}(z, u)] \mathcal{P}(u) du, \quad (2)$$

where $\mathcal{P}(u)$ is the distribution of the photons over their dimensionless escape time $u = t/t_{fp}$,

$$u_{max,\varepsilon}(z) = (3/\varepsilon) \ln(1 + \varepsilon/3z) \gg 1, \quad (3)$$

is a maximal number of scatterings related to the dimensionless energy $z = E/m_e c^2$.

$$z_0 = \psi^{(\varepsilon)}(z, u) = (\varepsilon/3) / [(1 + \varepsilon/3z) \exp(-\varepsilon u/3) - 1], \quad (4)$$

is the dimensionless photon energy $z_0 = E_0/m_e c^2$ at $u = 0$ and $\varepsilon \ll 1$ is a coefficient of the diverging term in the kinetic (Fokker-Planck) equation (see Eqs. 16, 17 in TSh05 and related discussion). In fact, ε is an average relative energy redshift per scattering. Below (see Eq. 12), we evaluate these values and verify them using results of our Monte Carlo simulations. We find that $\varepsilon \sim \beta/2\tau$ is of order of 10^{-2} for $\beta \lesssim 0.1$ and for τ of a few.

This result is a generalization of ST80 and TKB results. ST80 derived the spectra when the downscattering effects due to the recoil was taken into account. It should

be noted that the downscattering modification of the spectrum occurs when photons undergo multiple scatterings u . Thus we can expand the integrand function $W^{(\varepsilon)}(z, u) = e^{-4\varepsilon u/3}[\psi^{(\varepsilon)}(z, u)]\varphi[\psi^{(\varepsilon)}(z, u)]$ over u in formula (2):

$$W^{(\varepsilon)}(z, u) \approx W^{(\varepsilon)}(z, 0) + W_u^{(\varepsilon)'}(z, 0)u + W_u^{(\varepsilon)''}(z, 0)u^2/2 + W_u^{(\varepsilon)'''}(z, 0)u^3/3! + \dots \quad (5)$$

For the simplest case of the power-law incident spectrum and neglecting the diverging term in the kinetic (Fokker-Planck) equation ($\varepsilon = 0$) the resulting spectrum (Eq. 2) is as follows

$$\mathcal{F}_E(z) = \frac{A}{z} \int_0^{1/z} (1/z - u)^{\alpha-1} \mathcal{P}(u) du. \quad (6)$$

Using the expansion (5) one can obtain (see Appendix A, Eq. A6)

$$\begin{aligned} \mathcal{F}_E(z) = & Az^{-\alpha} [M_0(z^{-1}) + \frac{(1-\alpha)}{1!} z M_1(z^{-1}) + \frac{(1-\alpha)(2-\alpha)}{2!} z^2 M_2(z^{-1}) + \dots \\ & + \frac{(1-\alpha)(2-\alpha)\dots(n-\alpha)}{n!} z^n M_n(z^{-1}) + \dots], \end{aligned} \quad (7)$$

where

$$M_n(z^{-1}) = b \int_0^{1/z} u^n \exp(-bu) du \quad \text{for } n = 0, 1, 2 \dots \quad (8)$$

Note, the first term in the parenthesis of the right hand side $M_0(z^{-1}) = 1$ for $z \ll 1$ and the second term of that $(1-\alpha)zM_1(z^{-1})$ is positive if energy index of the primary photon spectrum $\alpha < 1$. Thus one can expect the photon accumulation bump at low energies for the downscattered power-law spectra for which the primary photon spectrum is quite hard (the energy index $\alpha < 1$). Indeed, in the pure scattering case the photon number is conserved, so if large numbers of the downscattered high energy photons are removed from the high energy part of the incident spectrum, then they should be seen at lower energies as a so called *downscattering* bump.

In Figures 4, 5 we present the Monte Carlo simulated spectra along with the analytical spectra (Eq. 7) for the power-law incident spectra for $\tau = 4$ and $\tau = 2$ respectively.

The downscattering (accumulation) bump and softening of spectrum at high energies are clearly seen in these spectra. As optical depth increases more prominent bumps are formed in the outflow. The softening of the analytic spectra due to the downscattering effect is well described by exponential decay of moments of the time distribution, $M_i(1/z)$ ($i = 0, 1, 2, \dots$) at higher energies (i.e. when $b/z > 1$), see Eqs. (8), (A9). The parameter b is only a free parameter to fit the analytical formula, we fix $\varepsilon = 0$ for which $u_{max} = 1/z$, see Eq. (3), namely $\lim_{\varepsilon \rightarrow 0} u_{max}^\varepsilon = 1/z$. For $\tau = 4$ the analytical spectra (7) perfectly represent

the simulated spectra for a wide range of the wind velocities $V = \beta c \lesssim 0.8c$. It is worth noting that we need not more than 6 terms of asymptotic series (7) to achieve the highest accuracy of the analytical spectra calculations.

For $\beta = 0.05, 0.1, 0.3, 0.8$ the best-fit parameters $b = 0.07, 0.07, 0.11, 0.45$ respectively. The inverse of b -parameter, $N_{av} = 1/b$ is an average number of scatterings undergone by the photons in the wind. For a faster wind the number of scatterings naturally decreases because photons are effectively taken by the outflow and less photons are scattered off outflow electrons. ST85, calculate b -parameters (and the average number of scatterings N_{av}) for spherical and plane (disk) geometry (Table 1, in ST85, where β corresponds to our value b). ST85 present their results for the static case i.e the zero bulk velocity case. Thus we should compare their results with our results when $\beta = 0.05, 0.1$. Moreover, our wind extended envelope of optical depth τ is equivalent to the disk of half-optical depth $\tau/2$. For example, for $\tau = 4$, our $b = 0.07$ should be related to 0.101 in ST85 for $\tau = 2$. As expected our b -value is smaller (or $1/b$ greater) than that in ST85, because the empty internal cavity of the wind envelope essentially amplifies the number of photon scatterings with respect to that in a plane disk of the same optical depth. The scattering effect of the cavity is suppressed when the wind velocity (or β) increases. For $\beta = 0.3$, the cavity effect and the wind velocity on scattering compensate each other. Our value of $b = 0.11$ is very close to that in ST85.

In Figure 5 we show the simulated spectra along with the analytical spectra for $\tau = 2$. One can notice that the best-fit analytical spectra slightly deviate from the simulated spectra at high energies. For $\beta = 0.05, 0.1, 0.3, 0.8$ the best-fit parameters $b = 0.13, 0.15, 0.21, 0.62$ respectively. ST85 give the corresponding value of $b = 0.234$ (related to our b -parameter for $\beta = 0.05$). From this comparison it is evident that the scattering effect of the cavity becomes stronger with the optical depth decrease. As expected, the analytical spectra as solutions of the diffusion problem in Thomson regime may depart from the Monte Carlo simulated spectra for $\tau \lesssim 2$ at high energies where the electron opacity is less than the Thomson opacity. The central source spectrum (dashed line) is slightly less modified by the scattering in the wind (see MC histogram for the simulated spectrum) than that using the diffusion spectrum (solid line).

Another interesting case is the downscattering modification of Comptonization spectrum (see e.g. ST80 and Titarchuk 1994). The incident Comptonization spectrum can be well fitted by a power-law spectrum with an exponential cutoff, namely

$$\varphi_{comp}(z) \approx Az^{-\alpha} \exp(-z/z_*). \quad (9)$$

where $z_* = E_*/m_e c^2$ is the dimensionless photon energy and the cutoff energy E_* is related to the Compton cloud electron temperature kT_e , namely $E_* \approx 2kT_e$. The downscattering modification of the spectrum, (see Eq. A8) can be written using the expansion (5). It can be

shown that for $\varepsilon = 0$ and $z_* \rightarrow \infty$ formula (A8) is reduced to formula (7). In Figures 6 and 7 we present the Monte Carlo simulated spectra for the power-law with exponential-cutoff incident spectra for $\tau = 4$, $\tau = 2$ respectively along with the analytically calculated spectra (see Eqs. A8, A20-A25). The MC simulated spectra are well described by the analytical model for all $\beta \lesssim 0.8$. It is worth noting that the downscattering bumps are not seen in either the simulated nor model spectra.

For $\tau = 4$ and $\beta = 0.1, 0.3, 0.5, 0.8$ the best-fit parameters are $b = 0.06, 0.10, 0.18, 0.38$ respectively. For $\tau = 2$ and the same β the best-fit parameters are $b = 0.14, 0.21, 0.30, 0.59$ respectively. It is worth noting that the values of b -parameter for small $\beta \lesssim 0.1$ is almost independent of the shape of the incident spectrum (within the error bar $\delta b = \pm 0.005$) and it depends on τ only.

Comparison of the simulated and analytically calculated spectra leads us to conclude that the simulated spectra can be well described by the analytical model with only one free parameter b that is related to the mean number of photon scattering in the wind ($N_{av} = 1/b$). It means that the continuum spectral formation in the pure scattering wind is dictated by the mean number of scatterings N_{av} only but that the value of N_{av} is determined by the combined effect of the wind optical depth τ and the dimensionless wind velocity β .

3.3. K_α -Line formation in the outflow

Another observational feature of the wind is the strong broad feature of K_α line in the spectrum. Recently, Shaposhnikov & Titarchuk (2006) demonstrate that these strong iron lines are present in all spectral states of Cyg X-1. Also they show that the equivalent width (EW) of the K_α line increases with the photon index Γ from about 150 eV in the low/hard state to about 1.3 keV in the high/soft and very soft states.

The X-ray photons of the central source illuminates the wind (see Fig. 1). The wind gas is heated by Compton scattering and photoionizations by photons coming from the central object and is cooled by radiation, ionization, and adiabatic expansion losses (LT04). The photons above the K-edge energy are absorbed and ionize iron atoms which leads to the formation of the strong K_α line. LT04 calculated ionization, temperature structure and the equivalent widths of Fe K_α line formed in the wind. For the wide set of parameters of the wind (velocity, the Thomson optical depth τ) and the incident Comptonization spectrum (the index and the Compton cloud electron temperature) they established that EW of the line should be about 1 keV and less for the line to be observed. LT04 also predicted that in this case the inner radius of the wind should be situated at $(10^3 - 10^4)/\tau_0$ Schwarzschild

radii away from the central object.

3.3.1. *The spectral line redshift in outflow. Analytical Description*

In Figure 1 we show the picture of the line photon propagation in the wind. At each consecutive scattering the line photon in average loses its energy, in other words it is redshifted. A photon emitted near the inner boundary and subsequently scattered by an electron moving with velocity \mathbf{V}_1 , is received by an electron moving with velocity \mathbf{V}_2 as shown in Fig. 1. The change in frequency is

$$\nu_2 = \nu_1 [1 + (\mathbf{V}_1 - \mathbf{V}_2) \cdot \mathbf{n}/c] \quad (10)$$

where \mathbf{n} is a unit vector along the path of the photon scattered at the next point.

We remind a reader that in the static and spherical-symmetric medium and where electrons experience a random (Brownian) motion only, the mean energy change per scattering, $\langle \Delta E \rangle$, for photons undergoing quite a few scatterings is proportional to square of electron velocity, namely $\langle \Delta E \rangle \propto (V/c)^2$ (see e.g. Rybicki & Lightman 1979 and ST80).

On the other hand for photons undergoing numerous scatterings in the bulk flow $\langle \Delta E \rangle$ is just proportional to V/c . [see Titarchuk, Mastihiadis & Kylafis 1997, Appendix D and TKB). In order to make estimate of the loss per scattering, one has to find the response of the energy operator of the diffusion kinetic equation (see TKB, Eqs. 3, 18) to a delta-function injection. In Appendix B1 we show that in this standard diffusion approximation $\langle \Delta E \rangle$ is proportional to the velocity divergence, namely

$$\langle \Delta E \rangle \approx -\frac{4}{3} \frac{\nabla(\mathbf{V}/c)}{\kappa} E_0 \sim \frac{8}{3} \frac{\beta}{\tau} E_0 \quad (11)$$

where κ is the scattering coefficient (or the inverse of the scattering mean free path). But this method provides rather a qualitative estimate of the redshift effect in the outflow than a quantitative one. The value of the numerical factor 4/3 in equation (11) is not precisely correct, which suggests that factor 4/3 should be replaced by the right one; however, the form of the exact equation actually depends on $\beta = V/c$ and τ in a more complex way. Formula (11) should be then taken only as an estimate.

A useful result of the $\langle \Delta E \rangle$ estimate is obtained using the scattering geometry method (see Appendix B2)

$$\langle \Delta E \rangle \approx -\beta f / (2\tau) \sqrt{1 - (f/2\tau)^2} E_0. \quad (12)$$

Below we utilize the MC simulations to show that the numerical factor f in formula (12) is about one. Comparison of Eqs. (11) and (12) leads us to conclude that $\langle \Delta E \rangle$ is proportional to β but that is overestimated in equation Eq. (11).

The average energy of photons escaping after $N_{av} = 1/b$ scatterings is

$$\langle E \rangle_{sc} = (1 + \langle \Delta E \rangle)^{1/b} E_0. \quad (13)$$

From here using formula (12) we obtain that

$$\langle E \rangle_{sc} = \{1 - \beta f / (2\tau) \sqrt{1 - (f/2\tau)^2}\}^{1/b} E_0. \quad (14)$$

3.3.2. MC simulated spectral lines in outflow. Evidence of the strong redshift effect in the outflow

We simulate line profiles for different optical depths of the wind. In Figure 8 (left hand side panel) we present examples of the line profiles for simulations where we take into account only the pure electron scattering in the flow, photo-electric absorption being neglected in these simulations. In Figure 8 (right-hand side panel) we present the spectral profile of the line obtained as a result of the electron scattering in the flow along with photo-electric absorption. When the X-ray continuum spectrum of the central source illuminates the wind the seed K_α -photons are formed in the innermost part of the wind. The photo-absorption profile as a function of energy, calculated by LT04, is related to the specific case of $\beta = 0.1$, $\alpha = 0.5$, $kT_e = 50$ keV for which the inferred LT04 model parameter $r_{in}\tau/L_{40} = 6 \times 10^{12}$ cm. The model and X-ray continuum parameters are the following: r_{in} is the outflow inner radius, L_{40} is the luminosity of the central source in units 10^{40} erg s^{-1} , α is the energy spectral index and kT_e is the electron temperature of the Comptonization spectrum (see details of the photo-absorption calculations in LT04). We find that the height scale of the source exponential distribution, H , is only a small fraction of the inner radius or in other words $H/r_{in} \sim 0.04\tau$ is a small fraction of the optical thickness of the outflow. Thus *the sources of K_α is distributed in the innermost part of the flow*. We simulate the line profiles for $\tau = 2, 4$, $kT_e = 0.1$ keV, $\beta = 0.1$, and for an initial seed photon energy $E_{ph} = 6.6$ keV.

One can clearly see the red-skewed part of the spectrum formed by photons undergoing multiple scatterings, along with the primary peak formed by photons escaping directly to the observer. The normalization of the direct non-scattering line component is suppressed for $\tau = 2$. The real normalizations are $A_N = 1.35 \times 10^6$, 1.29×10^6 for the diffusion and diffusion+absorption cases respectively.

In a situation, when the effect of the photon photoionization and absorption is taken into

account, the red wing of the line (for energies less than 4 keV) and blue wing (for energies higher 8 keV) have to be suppressed due to high photo-electric absorption opacities. Despite this photo-absorption suppression, the red-skewed shape of the line is retained. Thus one can conclude that *the red-skewed line profiles are intrinsic signatures of outward propagation of K_α -photons generated at the bottom of the outflow due to the outflow illumination by the X-ray hard radiation of the central source.*

In Figure 9 we show timing properties of the line propagation in the outflow for 5 energy bands for the pure scattering case. In the plot the time is given in the free path time units $t_{fp} = l/c$. Photons escaping from the bottom atmosphere without scattering are at 6.6 keV. The model parameters used here are $kT_e = 0.1$ keV, $\beta = 0.1$, $\tau = 4$ (upper panel), and $\tau = 2$ (lower panel). We show the arrival time of photons at the top of the cloud for five energy bands, in free path time units t_{fp} . Soft lags, low energy emission at later times are clearly seen.

It is also worth noting that TKB predict soft lags, namely that a photon of initial energy E_0 loses its energy with time, i.e. $E = \exp(-u_{\text{TKB}})E_0$ [compare with our formulas (12, 14)]. The dimensionless time variable (we call it as u_{TKB}) used there is a mathematical variable for a convolution method (see their Eq. 9). It can be interpreted as a product of the number of scatterings t/t_{fp} multiplied by the mean photon inelasticity $\langle \Delta E \rangle / E$ (see our Eq. 12), i.e. $u_{\text{TKB}} = (\langle \Delta E \rangle / E)(t/t_{fp})$.

The photon distribution with respect to escape time integrated over energies can be fitted with an exponential law $b \exp(-bt/t_{fp})$ (shown in Fig. 2). The values of $b = 0.057$ and $b = 0.144$ for $\tau = 4$ and $\tau = 2$ respectively (and consequently the average number of scatterings $N_{av} = 1/b$) are very close to b (or N_{av}) obtained from the best-fit analytical spectrum for the same values of β and τ .

We also check the analytical estimate of the average redshift of the line energy using formula (14) and that obtained from our simulations with the values $\langle E \rangle_{sc} = 4.56$ keV and $\langle E \rangle_{sc} = 5.27$ keV for $\tau = 4$ and $\tau = 2$ respectively. On the other hand keeping in mind the values of b , related to a given τ we can obtain the same values of $\langle E \rangle_{sc}$ as the simulated ones using formula (14) with $f = 1.3$, $f = 1.7$ for $\tau = 2$ and $\tau = 4$ respectively. These values of $f > 1$ are expected in the framework of our analytical estimate of $\langle E \rangle$. (see details of the derivation in Eq. (B11)). It is worth noting that now we can calculate $\varepsilon = \langle \Delta E \rangle / E_0$ that follows from formula (12) using f inferred from our simulations. They are $\varepsilon = 0.03$, and 0.04 for $\tau = 2, 4$ respectively and for $\beta = 0.1$.

In Figure 10 we present the emergent line profiles for different values of τ and β . Spectral lines as a function of τ are for $\beta = 0.1$, and that as a function of β for $\tau = 2$. The source

photons are generated at the bottom of the cloud and the cloud temperature is kept fixed at $kT_e = 0.1$ keV. The red wing of the line profile is insensitive to the temperature of the flow if $kT_e < 1$ keV. On the other hand, the blue wing becomes broader with kT_e , but its relative width is still smaller than that of the red wing. In fact, the blue wing is affected for energies higher than K-edge (> 8 keV) if the photo-absorption is taken into account (see the left lower panels of Fig. 10). In general, the photo-absorption narrows the line profile (compare the lines profiles in the upper and lower panels of Fig. 10).

The line profiles depend quite strongly on τ and β . The shape of the red wing below the broad peak (see Fig. 10) follows a power law with index which is a strong function of τ and β . Our calculated indices are in agreement with the TKB results for $\beta < 0.5$ and $\tau_{eff} = 3\beta\tau > 1$. In TKB, the photon indices are equal to $\Gamma = 2 + \lambda_k^2$, where λ_k^2 are eigenvalues calculated using their equation (30).

When $\beta \sim 1$ the spectrum of scattered photons becomes flat even for $\tau = 2$. The relativistic spherical outflow completely washes out the bump induced by scatterings (see the right panels of Fig. 10). However, for relatively small β , the power law tails still remain steep for higher τ (see the left panels of Fig. 10). This is very similar to the results obtained by TKB.

4. Comparison of MC simulated line profiles with the data

In Figures 11 and 12 (the left panel) we present the results of fitting our model to the XMM (EPIC) data of Wilms et al. (2001) obtained during the observation of the bright Seyfert 1 galaxy MCG-6-30-15. These observations were focused on the broad Fe K α line at ~ 6.4 keV. For MCG 6-30-15 we fit the continuum with a power law of index 1.8 and compare the residuals with our model. The best-fit parameters of the pure scattering model we found are $E_{ph} = 6.51$ keV, $kT_e = 0.1$ keV, $\tau = 1.2$, $\beta = 0.02$. We generated the primary photons at the bottom of outflow. If we take into account the LT04 model for the photo-absorption along with electron scattering, then the best-fit parameters become $E_{ph} = 6.51$ keV, $kT_e = 0.1$ keV, $\tau = 1.7$, $\beta = 0.02$.

The best-fit model spectrum is very similar to the steep spectrum presented in Fig. 10 for $\beta = 0.01$ (black curve in the lower panel). The quality of the fits strongly depends on the outflow optical depth τ and bulk velocity β . It is less sensitive to the outflow temperature kT_e unless $kT_e \lesssim 0.1$ keV. It is important to note that using our diverging outflow model we confirm Fabian's (1994) finding that velocity of the warm absorber outflow is about 5000 km s $^{-1}$ in MCG-6-30-15.

We fitted the red-skewed iron line profiles for four galactic sources XTE J1550-564, GRO J1655-40, Cyg X-1 and GRS 1915+105 obtained by Miller et al. (2004b). All of these data can be fitted by our model. In Figures 11 and 12 (the right hand panel) we show an example of these fits to the data. For GRO J1655-40 for the pure scattering model we find that optical depth $\tau = 2.0$ and an outflow velocity is $\beta = 0.1$, much higher than that for MCG 6-30-15 and $E_{ph} = 7.1$ keV. If we take into account the photo-absorption along with scattering in our model, then the best-fit parameters are $\tau = 3.3$, $\beta = 0.25$ and $E_{ph} = 7.1$ keV. It is worth noting that the fit in this case is not so good as that in the case of the pure scattering model. It can mean that the iron abundance in GRO J1655-40 is less than cosmic abundance. In fact, LT04 calculated the photoabsorption cross-sections for the cosmic abundances.

As we have pointed out, the MC simulated line profiles are independent of the outflow size and are determined by four parameters τ , β , kT_e and E_0 . The size of the outflow shell can be determined by timing characteristics such as variability timescales and time lags. Our model predicts soft time lags, i.e. the time lags become longer as energy decreases. Time lags are scaled with the light crossing time, t_{cross} , from one to a few t_{cross} . Unfortunately time lag information is not yet available for all sources analyzed. The only available information at present is the lack of the iron line variability with respect to the continuum for a number of extragalactic sources [Markovitz, Edelson & Vaughan (2003)]. Thus one can suggest that these line features are formed in a more extended configuration than the source of the continuum (which is presumably a Compton cloud close to the compact object). Here we demonstrate how our model can be used in the analysis of the line data. The detailed interpretation of the line data using our outflow model will be presented in a separate publication.

5. Outflow reprocessing of X-ray continuum spectra: MC simulated spectra

We also study the modification of the central source X-ray spectrum in the warm outflow as a result of photoionization and downscattering. In Figure 13 we present the simulations for different values of $\tau = 2, 4$ and $\beta = 0.1, 0.3$. The results of simulations are shown as $E^2F(E)$ diagrams, where $F(E)$ is a photon spectrum. In these simulations, the incident (central source) spectrum is approximated by the sum of two components: a blackbody shape radiation presumably coming from the inner part of the accretion disk, and a power-law with an exponential cutoff coming from the Compton cloud (corona). The parameters used for this input spectrum are the color temperature of the blackbody component $kT_{bb} = 1.2$ keV, the power-law photon index $\Gamma = 1.5$ (energy index $\alpha = 0.5$), and the cutoff $E_{cutoff} = 50$ keV. As shown in Comptonization theory (see e.g. ST80, Titarchuk 1994) the exponential cutoff energy E_{cutoff} of the unsaturated Comptonization spectrum is approximately $2kT_e$

where kT_e is the plasma temperature of the Compton cloud. The temperature of spherically symmetric wind is $kT_e = 0.1$ keV.

For the X-ray spectrum of the central source we assume that the photon numbers are the same for the blackbody and hard components. In fact, the ratio of the photon numbers depends on the illumination of the Compton cloud by the source of blackbody radiation.

The photoelectric effect is taken into account in these simulations. When a photoelectric event occurred, we drew a random number to firstly determine if this event occurs in the K shell of iron. The probability of fluorescence is about 30 %. The fluorescence photon is then propagated into the cloud in the same way as the input central object spectrum.

In the simulated spectra one can clearly see features of the strong fluorescent K_α line and the deep K-edge formed in the wind. The prominent bump around 25 keV is a combined effect of photoionization and downscattering in the wind. The wind modification of the spectra is very sensitive to the optical depth of the wind τ and β . For example, for a given $\beta = 0.1$ (or the wind velocity $0.1c$) the depth of K-edge is broader and much deeper for $\tau = 4$ than for $\tau = 2$. As expected the width of the line increases with β (compare the spectrum for $\beta = 0.1$ with that for $\beta = 0.3$). It is important to emphasize that the shape of K_α line consists of narrow and broad components. These narrow and broad line features of the line are really observed in Cyg X-1 (see review of the K_α line observations in Cyg X-1 in the introduction section of ST06).

The shape of the spectrum for $\tau = 4$ and $\beta = 0.3$ is very similar to the observed spectrum of Cyg X-3 (TSh05 and Trudolyubov, 2006, private communication). We present the interpretation of Cyg X-3 data based on the results of our simulations elsewhere.

6. Discussion and Conclusions

It is important to point out that Thomson optical depth of outflow is an order of unity when the mass outflow rate \dot{M}_{out} is an order of the Eddington mass accretion rate \dot{M}_{Edd} and higher (see e.g. formula 4 in King & Pounds 2003).

Recent *XMM-Newton* observations of bright quasars (Pounds et al., 2003a,b; Reeves et al., 2003) give strong evidence for powerful outflows from the nucleus with mass rates $\dot{M}_{out} \sim \dot{M}_\odot \text{ yr}^{-1} \sim \dot{M}_{Edd}$ and velocity $V \sim 0.1c$ (i.e. $\beta = 0.1$) in the form of blueshifted X-ray absorption lines. These outflows closely resemble those recently inferred in a set of ultraluminous X-ray sources with extremely soft spectral components (Mukai et al. 2003; Fabbiano et al. 2003). It is also worth noting the recent observations of the strong outflows

from GRO J1655-40 (Miller et al. 2006) and the Nucleus of the Seyfert 1 Galaxy NGC 3783 using an intensive HST/Chandra/FUSE monitoring (Crenshaw et al. 2004) and the recent Chandra observations of highly obscured AGN (Levenson et al. 2004) reported in the AAS HEAD meeting in 2004. In particular, Levenson et al. analyze new Chandra observations of three Compton thick Seyfert 2s with obscuring column densities that exceed 10^{24} cm^{-2} . They report that the Fe K_{α} line is very prominent in these examples with equivalent width > 1 keV. Thus one can conclude that powerful mass outflows from Eddington-limited accreting compact objects appear to be a very widespread phenomenon. King & Pounds (2003) and Begelman, King & Pringle (2006) argue that the powerful outflows may provide the high luminosity observed in quasars and ULXs, and imply that such objects have a major effect on their surroundings. They further suggest that the powerful outflow phenomena have barely been explored, and the field promises to be fruitful.

It is out of the scope of this paper to study the consequences of the X-ray radiation for hydrodynamics of these outflows. Our goal is to elaborate the spectroscopic tools for probing the outflow physical conditions such as column density (the outflow optical depth) temperature and iron ionization charge state. Moreover the photoionization modeling of the outflow (see LT04) permits the determination of its distance from the central black hole.

We have presented the Monte Carlo simulations of the radiative transfer of monochromatic photons and continuum photons within a diverging outflow, a problem which is also of observational interest, in view of the observations of broad, redshifted Fe lines and downscattering bumps (so called “reflection features”) in extragalactic and galactic black hole candidate spectra. We also provide an analytic description of the simulated spectra which allows us to understand, in detail, the effect of the downscattering modification of the central source spectrum. In the form presented the derived formulae of the resulting spectra can be easily used as an efficient analytical tool for the spectral data analysis. We demonstrate that the strength of the downscattering bump is determined by the average number of scattering that photons undergo in the wind. From our simulations of the pure scattering wind model we find that the average number of scattering $N_{av} = b^{-1}$ suffered by the photons in the wind of optical depth $\tau \gtrsim 2$ is $\gtrsim \tau^2$ for $\beta \lesssim 0.1$ (see §3 for details). On the other hand the average number of scatterings N_{av} decreases when the velocity of the wind increases. A larger fraction of the photons are rather carried out by the flow than scattered there when velocities are higher than $0.1c$.

The outflow leads to a redshift of the photon energy producing a broad, red component (see Fig. 1 for illustration of this redshift effect) not unlike those of the Fe K_{α} lines observed. We demonstrate analytically and numerically (using Monte Carlo simulations) that the mean photon energy change per scattering in the outflow $\langle \Delta E \rangle$ is the first order effect with

respect of V/c , namely $\langle \Delta E \rangle \propto -V/c$. We further emphasize that the red-skewed line features appear when the line photons are generated very close to the bottom of the outflow due to the outflow illumination by the X-ray hard radiation of the central source.

An important result of our simulations (see also TKB’s results) is the natural suppression of a blue wing in the iron line feature without the need to invoke any specific geometric arrangement for the emission. The illumination of the outflow from inside by the X-ray radiation, is natural for a compact source geometry, where the X-ray radiation originates from the innermost part of the source (a Compton cloud along with a disk). The powerful wind presumably starts in outskirts of the source (see Everett & Ballantyne 2004 for the wind model). In our model the red-wing photons have undergone numerous scatterings in an (effectively) optically thick medium, with an associated first order redshift in each scattering. It is not surprising that the blue wing, as a result of the second order $(v/c)^2$ effect, is weak for $kT_e \lesssim$ keV and $\beta = V/c \lesssim 0.1$.

This red-skewed line is a natural consequence of the first order Doppler effect in the presence of multiple scattering and photo-absorption events in the wind. It does not require any particularly fine tuned geometric arrangement.

LT04 find the self-consistent temperature and ionization structure of the wind shell as a function of the parameter (radius/luminosity, $r_{in}\tau/L_{40}$ where r_{in} is the inner outflow radius and L_{40} is X-ray luminosity in units of 10^{40} erg s $^{-1}$) for a given Thomson optical depth of the shell. It is evident that the ionization parameter L_{40}/nor^2 is constant through the shell (i.e. for $r > r_{in}$) if the velocity of the wind is constant through the flow. Thus the LT04 solution allows one to determine the size of the shell base for a given luminosity of which the red-skewed line is observed. LT04 derive the range of parameter r_{in}/L_{40} where the outflow-produced stable solution exist. The allowed r_{in}/L_{40} values are concentrated around $10^{12} - 10^{13}$ cm.

Our model predicts the soft lags to be a function of E/E_0 , β and τ . The combination of the red-skewed features along with the soft time lags that strongly depends on β , τ and kT_e are intrinsic signatures of any diverging outflow.

The demonstrated application of our outflow model to data points out a potentially powerful spectral diagnostic for probes of the outflow-central object connection in Galactic and extragalactic BH sources. Particularly, analyzing MCG-6-30-15 data (see §4) we infer that bulk outflow velocity is about 6000 km s $^{-1}$. On the other hand the OVII edge in the warm absorber of MCG-6-30-15 indicates that the flow along line of sight is about 5000 ± 1000 km s $^{-1}$ (Fabian et al. 1994). Thus using a new X-ray spectroscopic method [our diverging (outflow) model] we confirm the early finding (that used UV spectroscopy) that velocity of

the warm absorber outflow of MCG-6-30-15 is about 5000 km s⁻¹.

L.T. acknowledges the support of this work by the Center for Earth Observing and Space Research of the George Mason University. L.T. also appreciates productive discussions with Ralph Fiorito, Stuart Wick, Phil Uttley, Martin Laming and Chris Shrader. We also acknowledge discussion of the paper results with the referee and his/her constructive and interesting suggestions.

A. Downscattering spectrum. Derivation of Analytical Spectra

A.1. Power-law as a spectrum of the primary photons

Here we demonstrate how formula (2) can be analytically calculated using the steepest descent method. At first to illustrate the main idea of this derivation we consider the simplest case when $\varepsilon = 0$ and $\varphi(z) = z^{-\alpha}$ when

$$W^{(0)}(z, u) = (1/z - u)^{\alpha-1} \quad (\text{A1})$$

and integral (2) is presented by equation (6), where $\mathcal{P}(u) = b \exp(-bu)$. If we change the variable $v = (1/z - u)z$ under integral (6) then the integral can be rewritten as follows:

$$\mathcal{F}_E(z) = \frac{Abz^{-\alpha}}{z} \exp(-b/z) \int_0^1 v^{\alpha-1} \exp(bv/z) dv. \quad (\text{A2})$$

Because the dimensionless frequency $z = E/m_e c^2 \ll 1$ for the energy range of the interest ($E \ll 511$ keV) and $b \gtrsim 0.1$ there is a wide energy range where $\lambda = b/z$ is a big parameter. Then the integral in formula (A2) can be calculated analytically using the steepest descent method. In order to do it one should expand the integrand function $v^{\alpha-1}$ in the Taylor's series

$$v^{\alpha-1} = 1 + \frac{(1-\alpha)}{1!}(1-v) + \frac{(1-\alpha)(2-\alpha)}{2!}(1-v)^2 + \dots + \frac{(1-\alpha)(2-\alpha)\dots(n-\alpha)}{n!}(1-v)^n + \dots \quad (\text{A3})$$

near the point $v = 1$ where $\exp(bv/z)$ has a sharp maximum. It is worth noting that series (A3) converges for all $v < 1$ and thus the series presentation of the emergent spectrum (A2) is *exact* for any $\lambda = b/z$:

$$\begin{aligned} \mathcal{F}_E(z) = \frac{Abz^{-\alpha}}{z} \exp(-b/z) [& L_0(\lambda) + \frac{(1-\alpha)}{1!} L_1(\lambda) + \frac{(1-\alpha)(2-\alpha)}{2!} L_2(\lambda) + \dots \\ & + \frac{(1-\alpha)(2-\alpha)\dots(n-\alpha)}{n!} L_n(\lambda) + \dots], \end{aligned} \quad (\text{A4})$$

where

$$L_n(\lambda) = \int_0^1 (1-v)^n \exp(\lambda v) dv \quad \text{for } n = 0, 1, 2 \dots \quad (\text{A5})$$

If we introduce the new variable $u = (1-v)/z$ in integral (A5) then formula (A4) can be rewritten in the form

$$\begin{aligned} \mathcal{F}_E(z) = Az^{-\alpha} [& M_0(z^{-1}) + \frac{(1-\alpha)}{1!} z M_1(z^{-1}) + \frac{(1-\alpha)(2-\alpha)}{2!} z^2 M_2(z^{-1}) + \dots \\ & + \frac{(1-\alpha)(2-\alpha)\dots(n-\alpha)}{n!} z^n M_n(z^{-1}) + \dots], \end{aligned} \quad (\text{A6})$$

where $M_n(z^{-1})$ is defined by equation (8).

A.2. Power-law with exponential cutoff as a spectrum of primary photons

In the general case of the incident spectra and $\varepsilon > 0$ formula (2) for the emergent spectrum can be rewritten as

$$\mathcal{F}_\nu(z, \varepsilon) = \frac{b}{z} \int_0^1 W^{(\varepsilon)}[z, v u_{max, \varepsilon}(z)] \exp(-\lambda v) dv \quad (\text{A7})$$

where $\lambda = b u_{max, \varepsilon}(z) \gtrsim 1$ and $W^{(\varepsilon)}(z, u) = e^{-4\varepsilon u/3} [\psi^{(\varepsilon)}(z, u)] \varphi[\psi^{(\varepsilon)}(z, u)]$ and $u = v u_{max, \varepsilon}(z)$. Because the integrand has a sharp exponential maximum at $v = 0$ (or $u = 0$) one can expand the non-exponential function $W^{(\varepsilon)}(z, u)$ in series over v (or u). That leads to the following formula

$$\begin{aligned} \mathcal{F}_\nu(z, \varepsilon) = \frac{A}{z} [& W^{(\varepsilon)}(z, 0) M_0(u_{max, \varepsilon}) + W_u^{(\varepsilon)(1)}(z, 0) M_1(u_{max, \varepsilon})/1! + \\ & + W_u^{(\varepsilon)(2)}(z, 0) M_2(u_{max, \varepsilon})/2! + \dots + W_u^{(\varepsilon)(n)}(z, 0) M_n(u_{max, \varepsilon})/n! + \dots], \end{aligned} \quad (\text{A8})$$

where $W_u^{(\varepsilon)(n)}(z, u)$ is n th partial derivative of $W^{(\varepsilon)}(z, u)$ over u and the moments $M_n(x)$ ($x = u_{max, \varepsilon}$) of $\mathcal{P}(u)$ as follows

$$M_n(x) = -x^n \exp(-x) + n M_{n-1}(x)/b \quad \text{for } n = 1, 2 \dots \quad (\text{A9})$$

For example for $n=0, 1, 2$ we obtain

$$M_0(x) = 1 - \exp(-bx), \quad (\text{A10})$$

$$M_1(x) = -x \exp(-bx) + (1/b) M_0(x), \quad (\text{A11})$$

$$M_2(x) = -x^2 \exp(-bx) + (2/b) M_1(x). \quad (\text{A12})$$

Because

$$W_u^{(\varepsilon)(n)}(z, 0) = W_u^{(\varepsilon)}(z, 0) \prod_{i=0}^{n-1} [\ln W_u^{(\varepsilon)(i)}(z, u)]'_u(u=0) \quad (\text{A13})$$

and

$$W^{(\varepsilon)}(z, 0) = z\varphi(z) \quad (\text{A14})$$

the analytical formula (A8) for the emergent spectrum can be presented as

$$\mathcal{F}_\nu(z, \varepsilon) = \varphi(z) \left\{ M_0(u_{max, \varepsilon}) + \sum_{n=1}^{\infty} \left[\prod_{i=0}^{n-1} [\ln W_u^{(\varepsilon)(i)}(z, u)]'_u(u=0) \right] M_n(u_{max, \varepsilon})/n! \right\}. \quad (\text{A15})$$

Thus the resulting spectrum $\mathcal{F}_\nu(z, \varepsilon)$ is a product of the incident spectrum $\varphi(z)$ and the downscattering transformation function (expression in the curl parenthesis in Eq. A15) that depends on the properties of the outflow, velocity, optical depth via the parameter b .

In fact, the more convenient way to calculate the resulting spectrum $\mathcal{F}_\nu(z, \varepsilon)$ is to calculate the derivatives $W_u^{(\varepsilon)(n)}(z, u)$ explicitly using the factorized form of $W_u^{(\varepsilon)(1)}(z, u)$, namely

$$W_u^{(\varepsilon)(1)}(z, u) = W_u^{(\varepsilon)}(z, u)\Phi(z, u), \quad (\text{A16})$$

where

$$\Phi(z, u) = [\ln z_0 \varphi(z_0)]_u \quad (\text{A17})$$

and

$$\varphi(z_0) = z_0^{-\alpha} \exp(-z_0/z_*). \quad (\text{A18})$$

Using Eqs. (A17 , A18) we obtain a formula for $\Phi(z, u)$:

$$\Phi(z, u) = [\ln z_0 \varphi(z_0)]_u = -4\varepsilon/3 + \frac{1 - \alpha}{z_0} \frac{\partial z_0}{\partial u} - \frac{1}{z_*} \frac{\partial z_0}{\partial u}. \quad (\text{A19})$$

Then one can calculate $W_u^{(\varepsilon)(n)}(z, u)$ as follows

$$W_u^{(n)} = \sum_{i=0}^{n-1} C_{n-1}^i W_u^{(n-1-i)} \Phi_u^{(i)} \quad \text{for } n = 2, 3, \dots \quad (\text{A20})$$

where $C_n^k = n(n-1)..(n-k-1)/k!$ and $W_u^{(0)} = W$. Here and below we omit superscript ε in order to simplify the notation for $W_u^{(\varepsilon)(n)}(z, u)$ and its derivatives. We also introduce new notations $W_u^{(i)} = W^{(i)}(z, u)_u$ and $\Phi_u^{(i)} = \Phi^{(i)}(z, u)_u$.

Because

$$\frac{\partial z_0}{\partial u} = (\varepsilon/3)z_0 + z_0^2 \quad (\text{A21})$$

we can write Eq.(A19) as

$$\Phi(z, u) = -4\varepsilon/3 + (1 - \alpha)(\varepsilon/3 + z_0) - \frac{1}{z_*} \frac{\partial z_0}{\partial u} \quad (\text{A22})$$

and find the derivatives of $\Phi(z, u)$ as

$$\Phi_u^{(n)}(z, u) = (1 - \alpha) \frac{\partial^n z_0}{\partial u^n} - \frac{1}{z_*} \frac{\partial^{n+1} z_0}{\partial u^{n+1}} \quad \text{for } n = 1, 2, 3... \quad (\text{A23})$$

The second and higher derivatives of z_0 over u are

$$\frac{\partial^2 z_0}{\partial u^2} = (\varepsilon/3) \frac{\partial z_0}{\partial u} + 2z_0 \frac{\partial z_0}{\partial u}, \quad (\text{A24})$$

$$\frac{\partial^n z_0}{\partial u^n} = (\varepsilon/3) \frac{\partial^{n-1} z_0}{\partial u^{n-1}} + 2 \sum_{i=0}^{n-2} C_{n-2}^i \frac{\partial^i z_0}{\partial u^i} \frac{\partial^{n-1-i} z_0}{\partial u^{n-1-i}} \quad \text{for } n = 3, 4... \quad (\text{A25})$$

Now all derivatives $W_u^{(n)}$ in Eq.(A20) can be calculated very easily because $z_0 = z$ at $u = 0$ by definition.

B. The mean photon energy change in the bulk outflow. Analytical evaluations

B.1. Diffusion method

There is a standard procedure to estimate the energy gain and loss per scattering using diffusion approximation (Prasad et al. 1988 and Titarchuk, Mastihiadis & Kylafis 1997, Appendix D). Let us assume that in the initial moment $t = 0$ the monochromatic line of energy E_0 emits at any point of the scattering medium (outflow). The energy change of the line $\langle \Delta E \rangle$ due to scattering can be found using the time-dependent diffusion kinetic equation:

$$\frac{\partial n}{\partial u} = L_r n + L_\nu n \quad (\text{B1})$$

where $n(r, \nu)$ is the photon occupation number, L_r , L_ν the space and energy operators respectively (see TKB, Eq. 3) and $u = \kappa ct$ is the time measured in units of mean time between scatterings (see Rybicki & Lightman 1979, ST80). Our goal is to find a small change of the radiation field background which at the initial moment is

$$z^3 n|_{u=0} = z^3 n_0 = z\delta(z - z_0). \quad (\text{B2})$$

The energy change per scattering $\langle \Delta z \rangle = \langle \Delta E \rangle / m_e c^2$ can be found by multiplication of the kinetic equation (B1) by z^3 , substitution of equation (B2) in the right hand side and integration over z . Thus we have

$$\frac{\delta z}{\delta u} = \langle \Delta z \rangle = \int_0^\infty \frac{1}{3} \frac{\nabla(\mathbf{V}/c)}{\kappa} z^4 \frac{\partial n}{\partial z} dz, \quad (\text{B3})$$

where $\delta z / \delta u$ is a photon energy change per scattering.

Integration by parts gives

$$\langle \Delta z \rangle = -\frac{4}{3} \frac{\nabla(\mathbf{V}/c)}{\kappa} \int_0^\infty z^3 n_0 dz. \quad (\text{B4})$$

Substituting $z^3 n_0 = z\delta(z - z_0)$ (see Eq. (B2) in this equation, we obtain

$$\langle \Delta E \rangle = -\frac{4}{3} \frac{\nabla(\mathbf{V}/c)}{\kappa} E_0. \quad (\text{B5})$$

Because

$$\nabla(\mathbf{V}/c) = \frac{2\beta}{r} \quad (\text{B6})$$

and $\kappa r = \sigma_T n_e r \approx \tau$ for the electron number density of the constant velocity wind we can rewrite equation (B5) in the form

$$\langle \Delta E \rangle \approx -\frac{8}{3} \frac{\beta}{\tau} E_0. \quad (\text{B7})$$

B.2. Geometry of photon scattering in the outflow

In this section we evaluate $\langle \Delta E \rangle$ using equation (10) and geometry of photon scattering in the outflow. Ultimately, we should calculate the mean of the scalar product of $(\mathbf{V}_1 - \mathbf{V}_2) \cdot \mathbf{n}/c$ (\mathbf{n} is a unit vector along the path of the photon scattered at the next point, see Fig. 1).

The length of the vector

$$|\Delta \mathbf{V}| = |\mathbf{V}_1 - \mathbf{V}_2| = 2V \sin \theta/2 \approx v \sin \theta \quad \text{for } \theta < 1 \quad (\text{B8})$$

where θ is an angle between \mathbf{V}_1 and \mathbf{V}_2 . Let l is the mean free path between two consecutive scatterings at r_1 and r_2 (see Fig. 1) then

$$\cos \theta = \frac{r_1^2 + r_2^2 - l^2}{2r_1 r_2}. \quad (\text{B9})$$

If $|r_1 - r_2|/r_1 = \Delta r/r < 1$ ($r_1 \approx r_2 = r$) and $\Delta r < l^2/2r$ then we can estimate $1 - \cos \theta$ as follows

$$1 - \cos \theta \approx (l/r)^2/2, \quad (\text{B10})$$

Thus we can find that

$$\sin \theta \approx l/r = 1/(N_e \sigma_T r) = r/(r_{in} \tau) \sim f/\tau \quad (\text{B11})$$

when $l/r < 1$ and where the numerical factor $f \gtrsim 1$. The precise value of the factor f can be evaluated using our MC simulations. To derive formula (B11) we use the electron number distribution of the constant velocity wind (see formula 1).

The cosine of the angle γ between $\Delta \mathbf{V} = (\mathbf{V}_1 - \mathbf{V}_2)$ and \mathbf{n} is

$$\cos \gamma = \cos \psi \cos(\pi - \theta/2) + \sin \psi \sin(\pi - \theta/2) \cos(\varphi - \varphi_0) \quad (\text{B12})$$

where ψ is a zenith angle between vector \mathbf{n} and the normal to vector \mathbf{V}_1 directed toward vector \mathbf{V}_2 and φ and φ_0 are meridian (longitudinal) angles of \mathbf{n} and ΔV respectively. Then the mean value of $\cos \gamma$ over half of sphere located to the left from the vector \mathbf{V}_1 is calculated as follows

$$\langle \cos \gamma \rangle = \frac{1}{2\pi} \int_0^{2\pi} d\varphi \int_0^{\pi/2} \cos \gamma \sin \psi d\psi = -\frac{1}{2} \cos(\theta/2). \quad (\text{B13})$$

Thus using Eq.(10) and Eqs. (B8-B13) one can relate the mean energy change per scattering, $\langle \Delta E \rangle$, for photons undergoing quite a few scatterings in the flow with β as follows:

$$\langle \Delta E \rangle \approx -\beta f/(2\tau) \sqrt{1 - (f/2\tau)^2} E_0. \quad (\text{B14})$$

REFERENCES

- Blandford, R.D. & Payne, D.G. 1981, MNRAS, 194, 1033
- Begelman, M.C., King, A.R., & Pringle, J.E. 2006, MNRAS, 370, 399
- Crenshaw, D.M., et al. 2004, HEAD meeting in New Orleans, BAAS, 36, 32.02
- Everett, J.E., & Ballantyne, D.R. 2004, ApJ, 615, L13
- Fabbiano, G., et al. 2003, ApJ, 591, 843
- Fabian A.C., et al. 1994, PASJ, 46, L59
- Gilfanov, M., & Churazov, E. & Revnivtsev, M. 1999, A&A, 352, 182 (GCR99)
- Kallman, T.R., Palmeri, P., Bautista, M.A. et al. 2004, ApJS, 155, 675
- King, A.R., & Pounds, K.A. 2003, MNRAS, 345, 657
- Laming, J.M. & Titarchuk, L. 2005, ApJ, 615, L121 (LT04)
- Laurent, P. & Titarchuk, L. 2001, ApJ, 562, L67
- Laurent, P. & Titarchuk, L. 1999, ApJ, 511, 289 (LT99)
- Levenson, N.A., Weaver, K.A., Heckman, T.M., Krolik, J.H., & Zycki, P.T. 2004, HEAD meeting in New Orleans, BAAS, 36, 32.04
- Lifshitz, E.M. & Pitaevsky, L.P. 1981, Physical Kinetics (Oxford: Pergamon Press)
- Magdziarz, P., & Zdziarski, A.A. 1995, MNRAS, 273, 837 (MZ95)
- Markowitz, A., Edelson, R., & Vaughan, S. 2003, ApJ, 598, 935
- Miller, J. et al. 2006, Nature, 441, 953
- Miller, J. et al. 2004a, ApJ, 601, 450
- Miller, J. et al. 2004b, in *Proceedings of 10th Marcel Grossmann Meeting, Ed. R. Ruffini*, astro-ph/0402101
- Mukai, K., Pence, W.D., Snowden, S.L., & Kuntz, K.D., 2003, ApJ, 582, 184
- Nandra, K. et al. 1997, ApJ, 477, 602
- Nobili, L. Turolla, R. & Zampieri, L. 1993, ApJ, 404, 686

- Payne, D.G., & Blandford, R.D. 1981, MNRAS, 196, 781 (PB81)
- Pottschmidt, K., et al. 2003, A&A, 407, 1039
- Pounds, K.A., Reeves, J.N., King, A.R., Page, K.L., O’Brien, P.T., & Turner, M.J.L. 2003a, MNRAS, 345, 705
- Pounds, K.A., Reeves, J.N., King, A.R., Page, K.L., O’Brien, P.T. 2003b, MNRAS, 346, 1025
- Prasad, M.K., Shestakov, A.V., Kershaw, D.S., Zimmerman, G.B. 1988, J. Quant. Spectrosc. Radiat. Transfer, 40, 29
- Reeves, J.N., O’Brien, P.T., & Ward, M.J. 2003, ApJ, 593, 65
- Rybicki, G.B., & Lightman, A.P. 1979, Radiative Processes in Astrophysics (John Wiley & Sons: New York)
- Shaposhnikov, N.. & Titarchuk, L. 2006, ApJ, 643, 1098 (ST06)
- Strohmayer, T.E. & Brown, E.F. 2002, ApJ, 566, 1045
- Sunyaev, R.A. & Titarchuk, L.G. 1985, A&A, 143, 374 (ST85)
- Sunyaev, R.A. & Titarchuk, L.G. 1980, A&A, 86, 121 (ST80)
- Tanaka, Y., et al. 1995, Nature, 375, 659
- Titarchuk, L.G. 1994, ApJ, 434, 570
- Titarchuk, L., & Shrader, C.R. 2005, ApJ, 623, 362 (TSh05)
- Titarchuk, L., Kazanas, D. & Becker, P.A. 2003, ApJ, 598, 411 (TKB)
- Titarchuk, L., Mastichiadis, A. & Kylafis, N.D. 1997, ApJ, 487, 834
- Uttley, P. et al. 2004, MNRAS, 347, 1345
- Vaughan, S. & Fabian, A.C. 2003, MNRAS, 348, 1415
- Wilms, J. et al. 2001, MNRAS, 328, L27

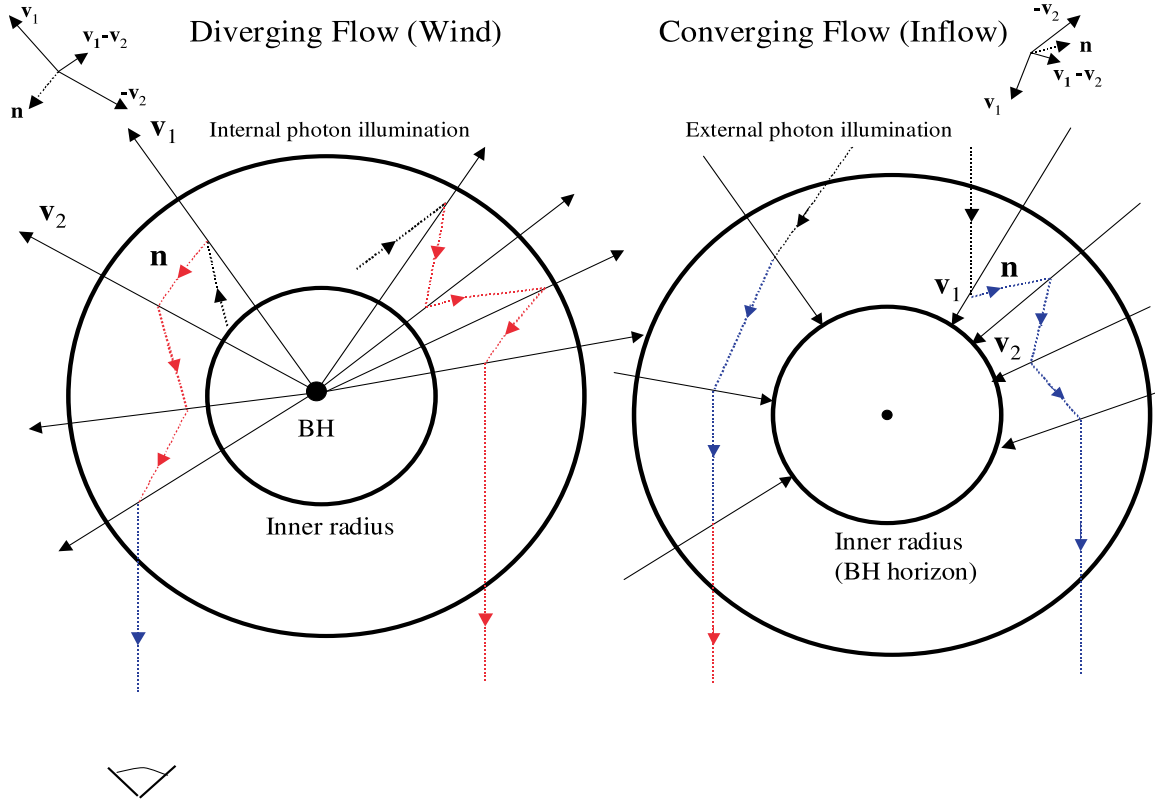


Fig. 1.— On the left side: Schematic diagram showing wind geometry. The relatively cold outflow (wind) originates at the inner radius. The optical depth of the wind in the Fe K continuum and the electron scattering optical depth of the wind are of order unity. A photon emitted near the inner boundary and subsequently scattered by an electron moving with velocity \mathbf{V}_1 , is received by an electron moving with velocity \mathbf{V}_2 as shown. The change in frequency is $\nu_2 = \nu_1 (1 + (\mathbf{V}_1 - \mathbf{V}_2) \cdot \mathbf{n}/c)$ where \mathbf{n} is a unit vector along the path of the mv photon scattered at the next point. In a diverging flow $(\mathbf{V}_1 - \mathbf{V}_2) \cdot \mathbf{n}/c < 0$ and photons are successively redshifted, until scattered to an observer at infinity. The color of photon path indicates the frequency shift in the rest frame of the receiver (electron or the Earth observer). On the right side: In a converging flow $(\mathbf{V}_1 - \mathbf{V}_2) \cdot \mathbf{n}/c > 0$ and photons are blueshifted.

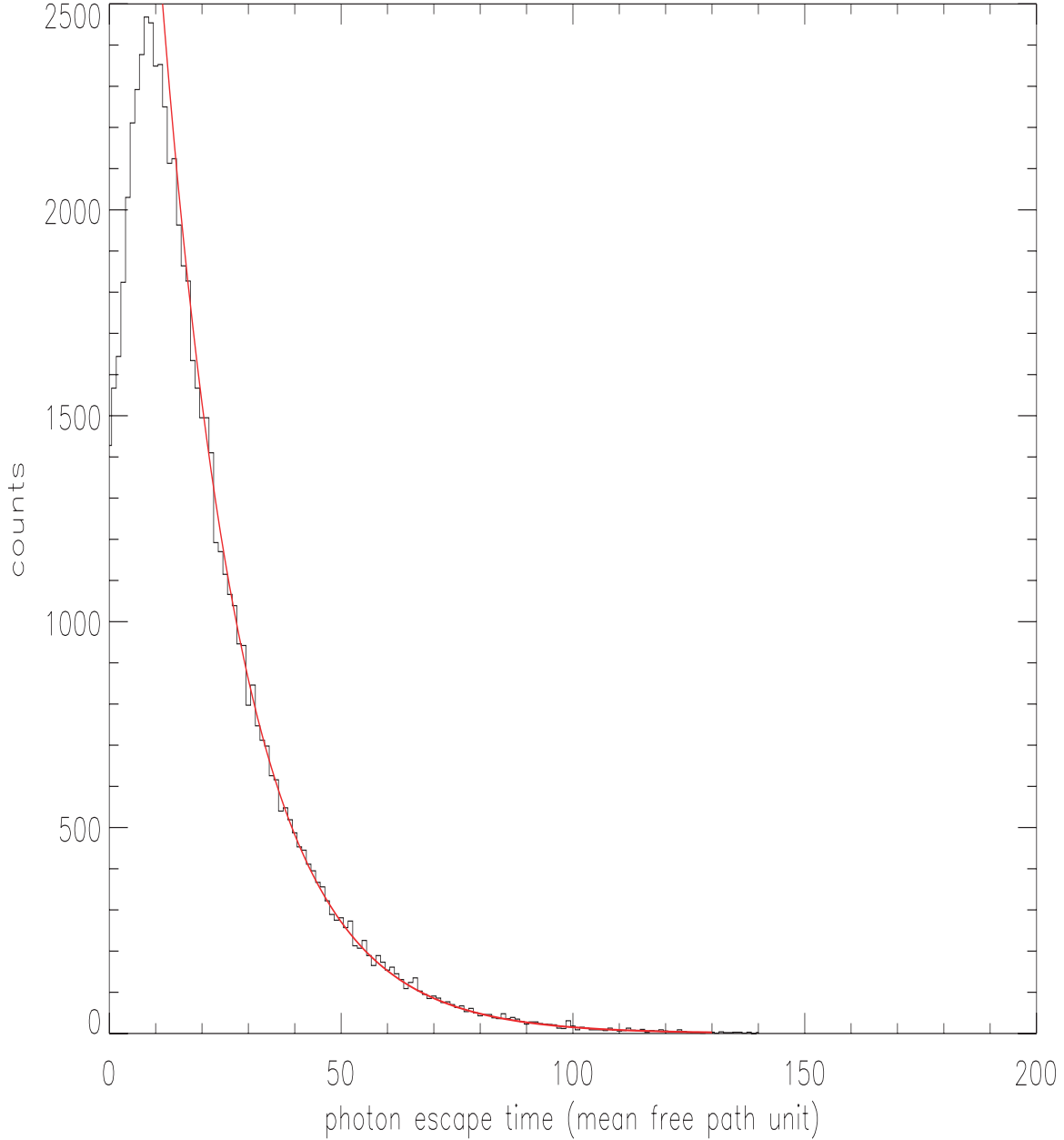


Fig. 2.— Timing properties of the outflow. The photon distribution over escape time $\mathcal{P}(t/t_{fp})$, where $t_{fp} = l/c$ is a free path time. This simulation is made for the incident spectrum as a power-law with exponential cutoff for $kT_e = 0.1$ keV, $\tau = 4$ and $\beta = 0.1$. It is worth noting that the index $b = 0.057$ of the exponential distribution $\exp(-bt/t_{fp})$ (red line) is very close to the best-fit parameter values 0.06 ± 0.005 for the energy spectrum. We find that in all cases the best-fit parameter b obtained from the photon distribution over escape time is very close to b obtained from the best-fit analytical spectrum.

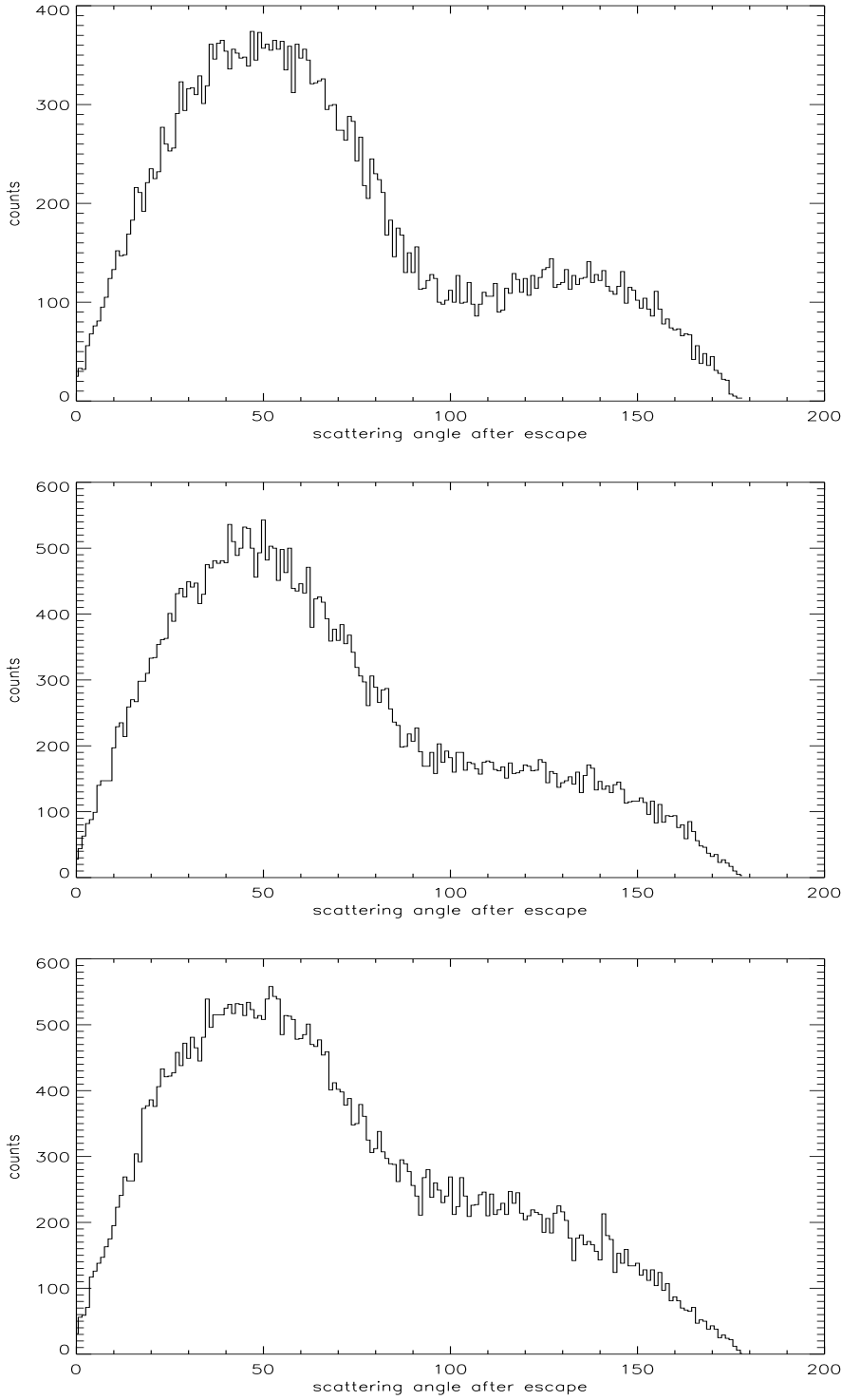


Fig. 3.— The outflow shell is radially illuminated by the central source radiation. Photon distribution over deflecting angles with respect to the radial direction of the incident photons. Upper panel: $\tau = 1$, middle panel: $\tau = 2$ and lower panel: $\tau = 4$ and $\beta = 0.1$. In fact, we find in our simulations that the angle distribution of the scattering component weakly depends on τ . But there is a big difference in the normalization of the direct (non-scattering) component A_N for which the ratio of $A_N(\tau = 4)/A_N(\tau = 1) = \exp(-4 + \tau)$.

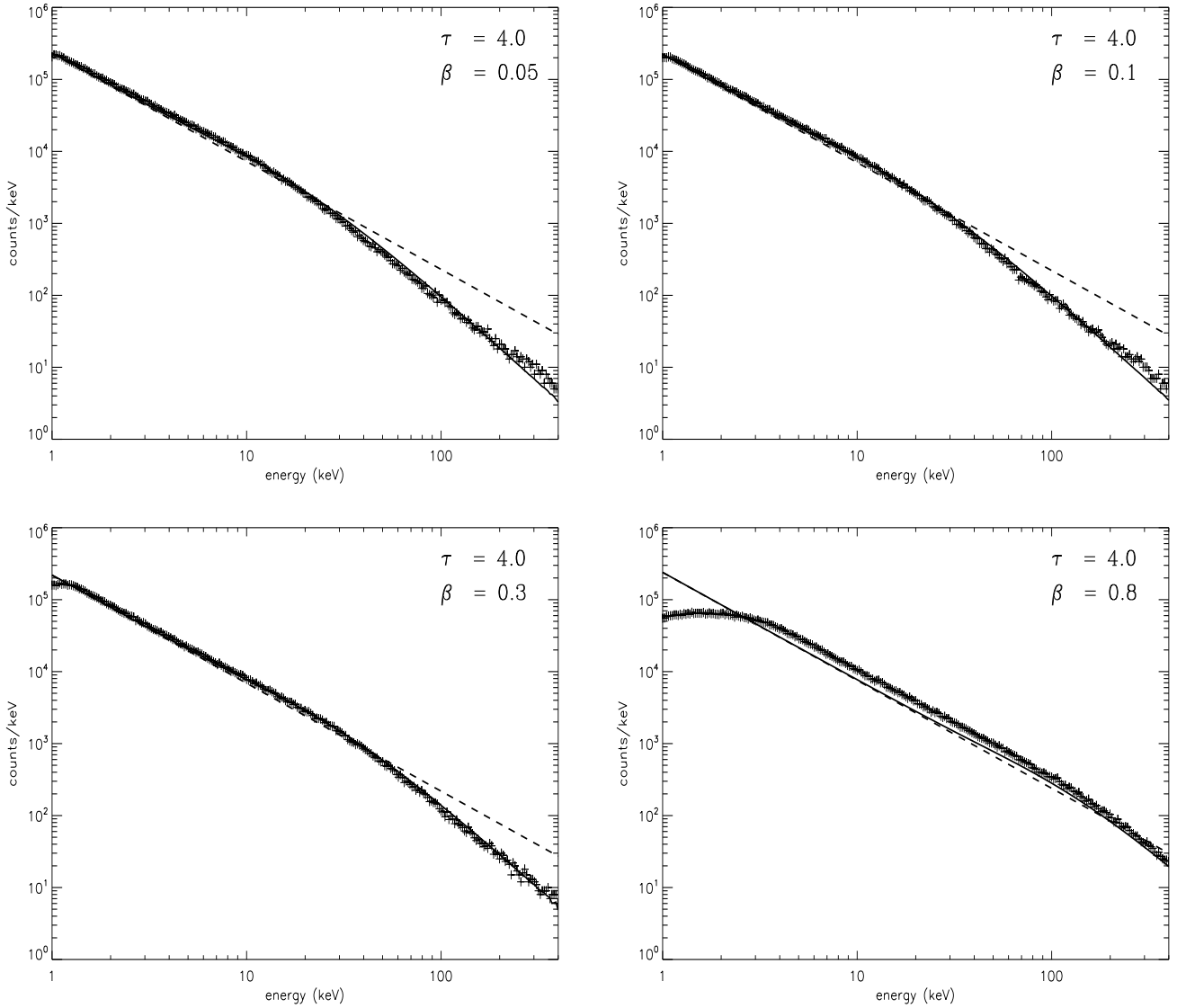


Fig. 4.— Emerging spectrum of a compact object through an outflowing plasma. The incident spectrum inside the outflowing plasma is taken to be a power-law $\varphi(E) \propto E^{-\alpha}$ for which the energy index $\alpha = 0.5$. Outflow parameters are $kT_e = 0.1$ keV, $\tau = 4$ and $\beta = 0.05, 0.1, 0.3, 0.8$. The photon emerging spectrum (cross points) is compared to the incident spectrum (dash line) and the analytical downscattering spectrum (solid line) (see Eq. 7). For $\beta = 0.05, 0.1, 0.3, 0.8$, the best-fit parameters are $b = 0.07, 0.07, 0.11, 0.45$ respectively. For all cases we fix the $\varepsilon = 0$. One can clearly see a bump in the MC simulated and analytical spectra, in the low energy band around 10 keV for all $\beta \lesssim 0.3$. Indeed, in the purely diffusive case that is shown in this plot, the photon number is conserved, so the downscattered high energy photons, which are removed from the high energy part of the incident spectrum, are detected at lower energy.

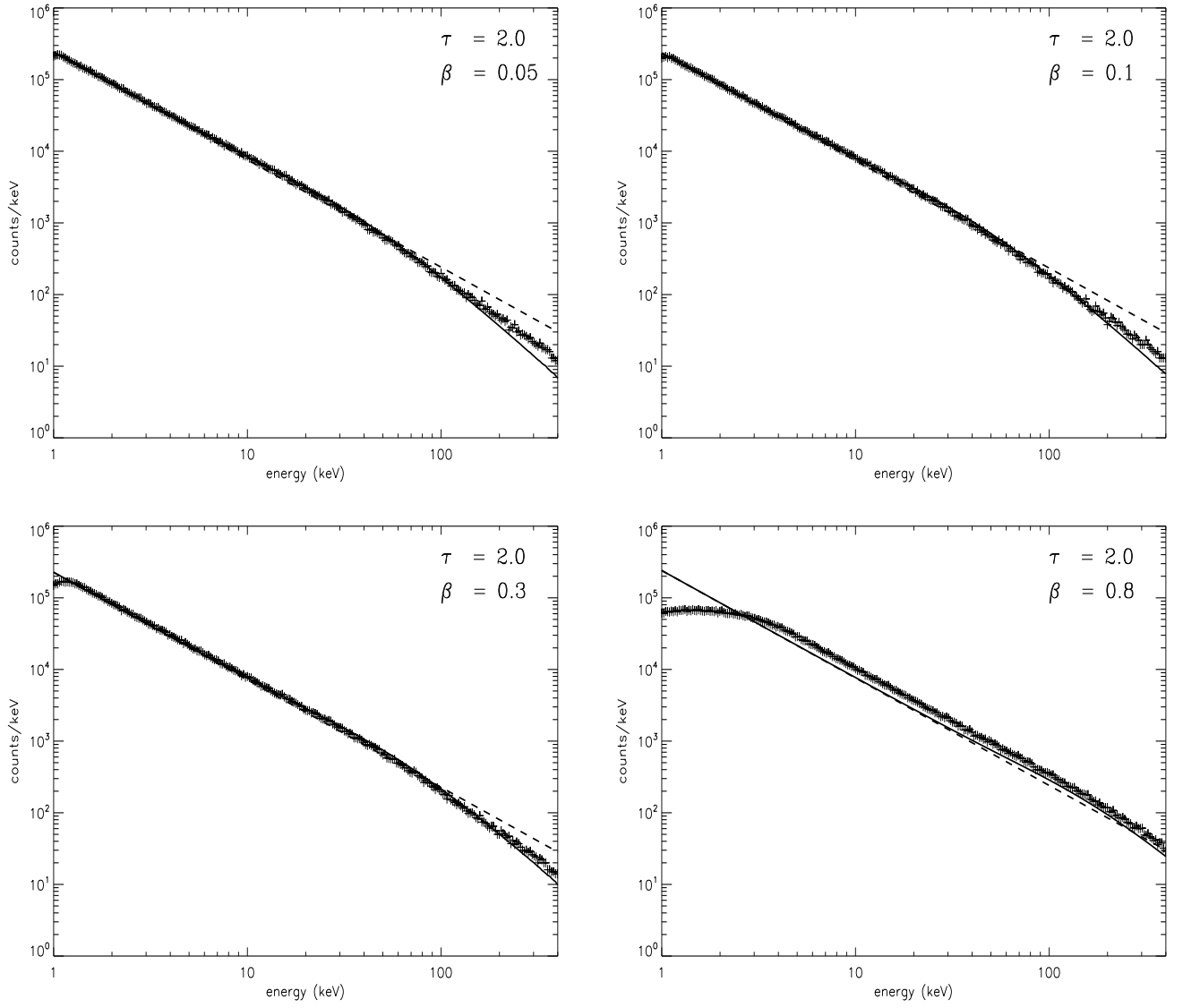


Fig. 5.— The same as in Fig. 4 for $\tau = 2$. For $\beta = 0.05, 0.1, 0.3, 0.8$, the best-fit parameters are $b = 0.13, 0.15, 0.21, 0.62$ respectively.

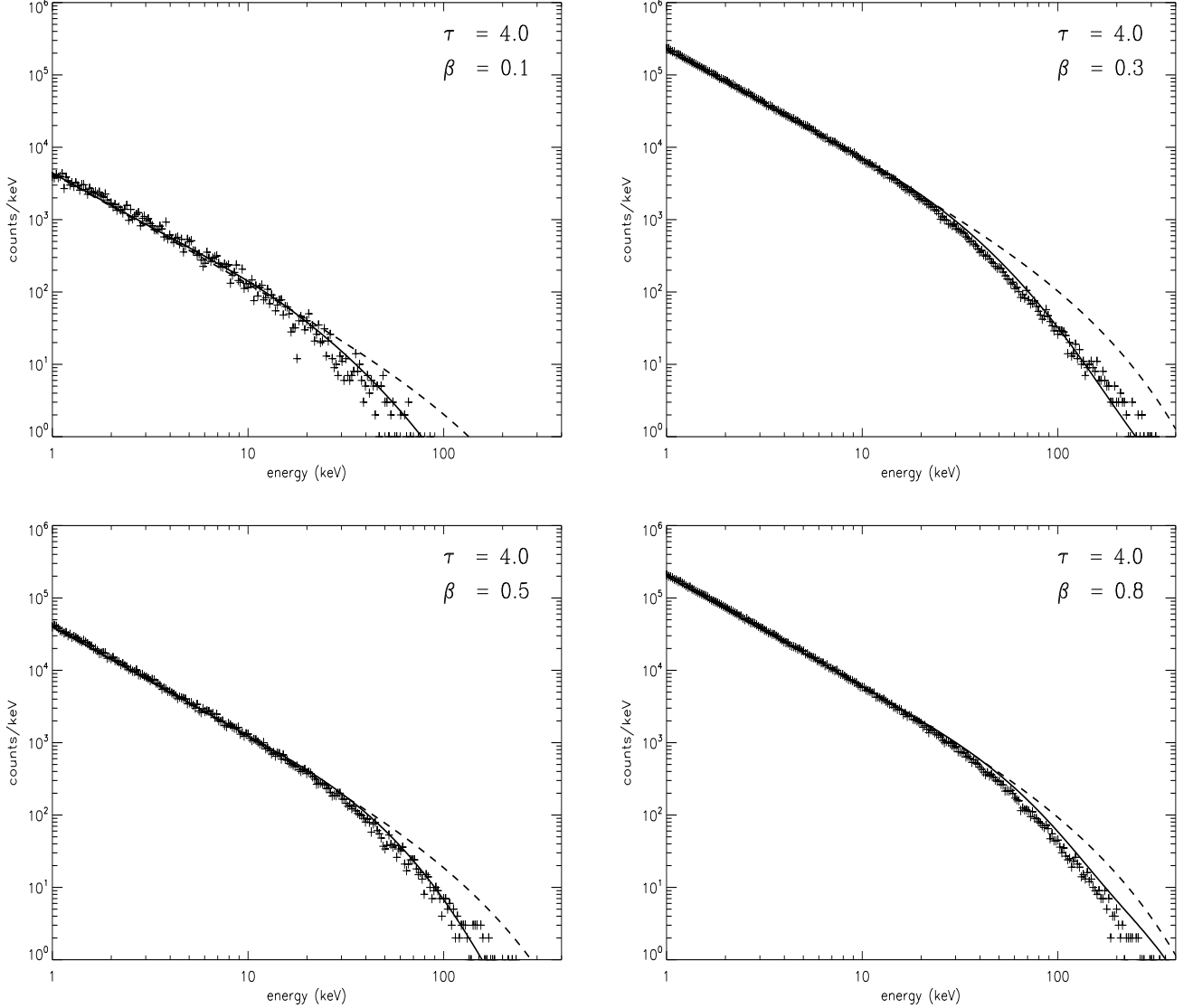


Fig. 6.— Emerging spectrum of a compact object through an outflowing plasma. The incident spectrum inside the outflowing plasma is taken to be $\varphi_{comp}(E) \propto E^{-\alpha} \exp(-E/E_*)$ (see Eq. 9) where energy index $\alpha = 0.5$ and high energy cutoff at $E = E_* = 130$ keV. Outflow parameters are $kT_e = 0.1$ keV, $\tau = 4$. The photon emerging spectrum (cross points) is compared to the incident spectrum (dash line) and the analytical downscattering spectrum (solid line) (see Eq. A8). For $\beta = 0.1, 0.3, 0.5, 0.8$, the best-fit parameters are $b = 0.06, 0.10, 0.18, 0.38$ respectively. *The low energy downscattering bump effect is not seen in the emergent spectra.*

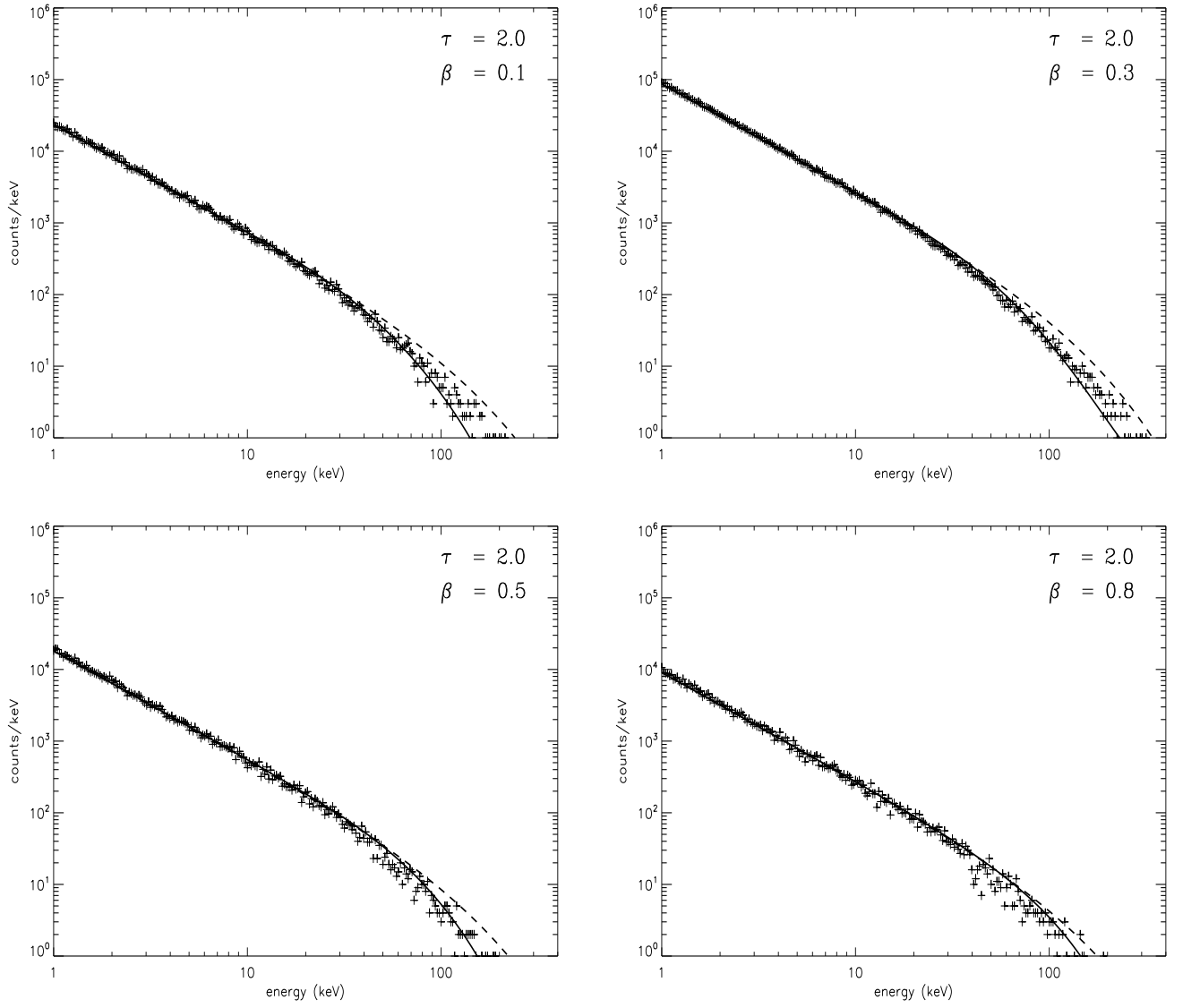


Fig. 7.— The same as in Fig. 6 for $\tau = 2$. For $\beta = 0.1, 0.3, 0.5, 0.8$, the best-fit parameters are $b = 0.14, 0.21, 0.30, 0.59$ respectively.

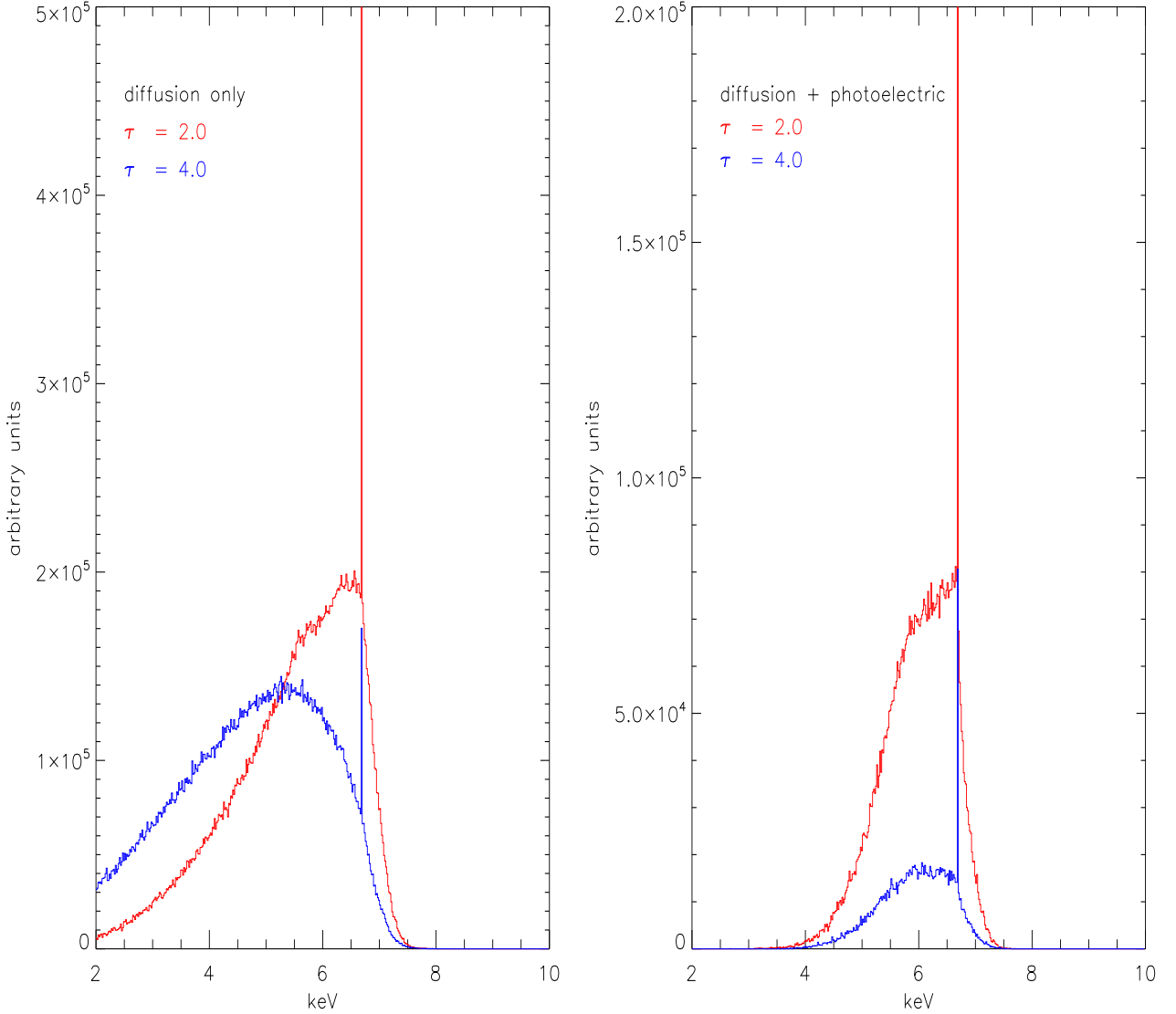


Fig. 8.— Line profiles as a function of τ (for $\beta = 0.1$). Primary photons are generated at the bottom of outflow. On the left-hand side : the line profiles for the pure scattering case and on the right-hand side : that for scattering plus absorption case. In each case, the fixed parameters are $E_{ph} = 6.6$ keV, $kT_e = 0.1$ keV. The normalization of the direct non-scattering line component is suppressed for $\tau = 2$. The real normalizations are $A_N = 1.35 \times 10^6$, 1.29×10^6 for the diffusion and diffusion+absorption cases respectively.

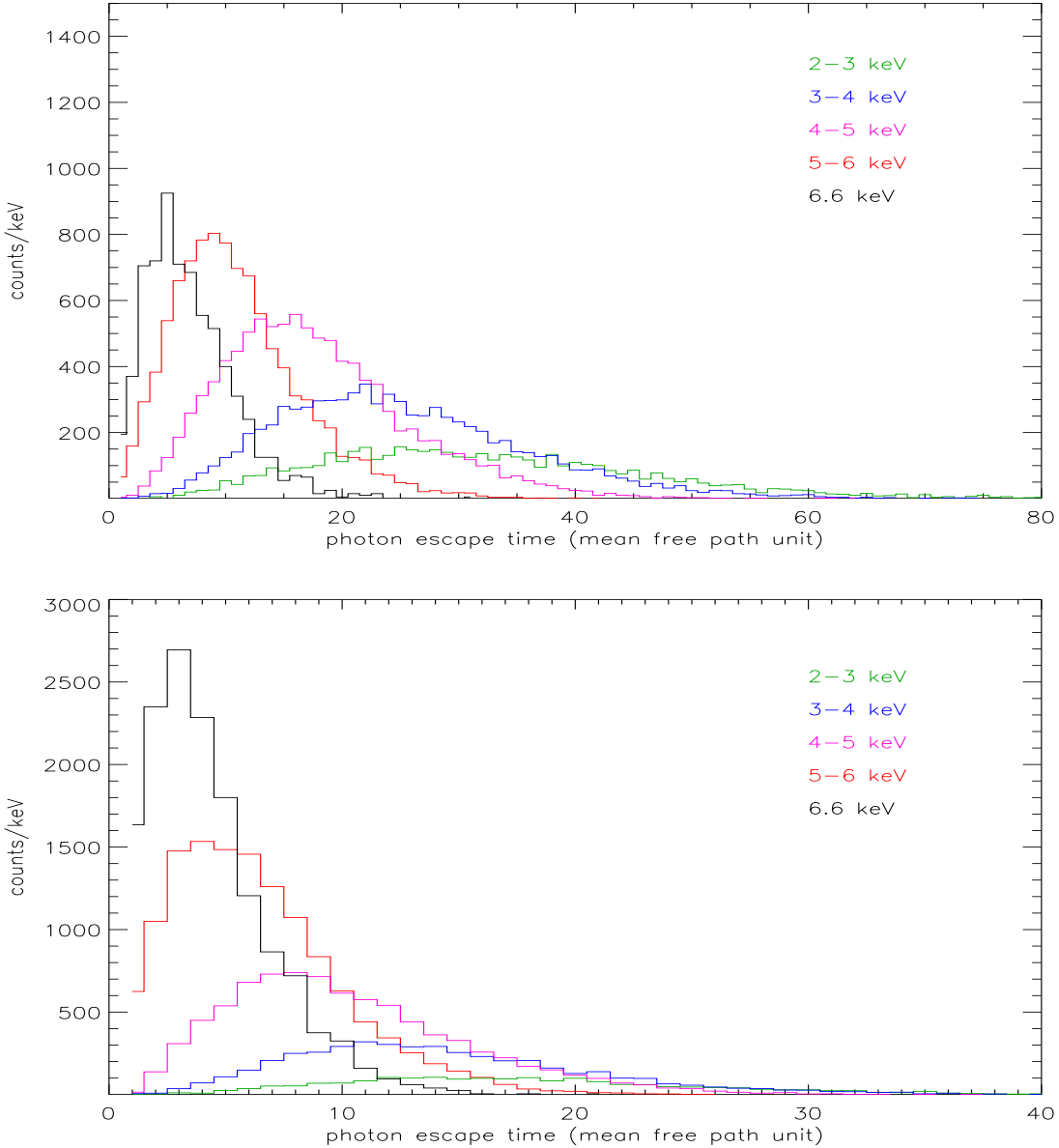


Fig. 9.— Timing properties of the line propagation in the outflow. A flash of monochromatic photons at 6.6 keV is simulated, and propagated. Photons escaping from the bottom atmosphere without scattering are at 6.6 keV (see Fig. 1). The model parameters used here are $kT_e = 0.1$ keV, $\beta = 0.1$ and $\tau = 4$ (upper panel), and $\tau = 2$ (lower panel). We show the arrival time of photons at the top of the cloud for five energy bands, in free path time units $t_{fp} = l/c$. Soft lags, low energy emission at later times are clearly seen. The photon distribution over escape time integrated over energies can be fitted with an exponential law $b \exp(-bt/t_{fp})$ (shown in Fig. 2). The values of $b = 0.057$ and $b = 0.144$ for $\tau = 4$ and $\tau = 2$ respectively (and consequently average number of scatterings $N_{av} = 1/b$) are very close to b (or N_{av}) obtained from the best-fit analytical spectrum for the same values of β and τ (see text).

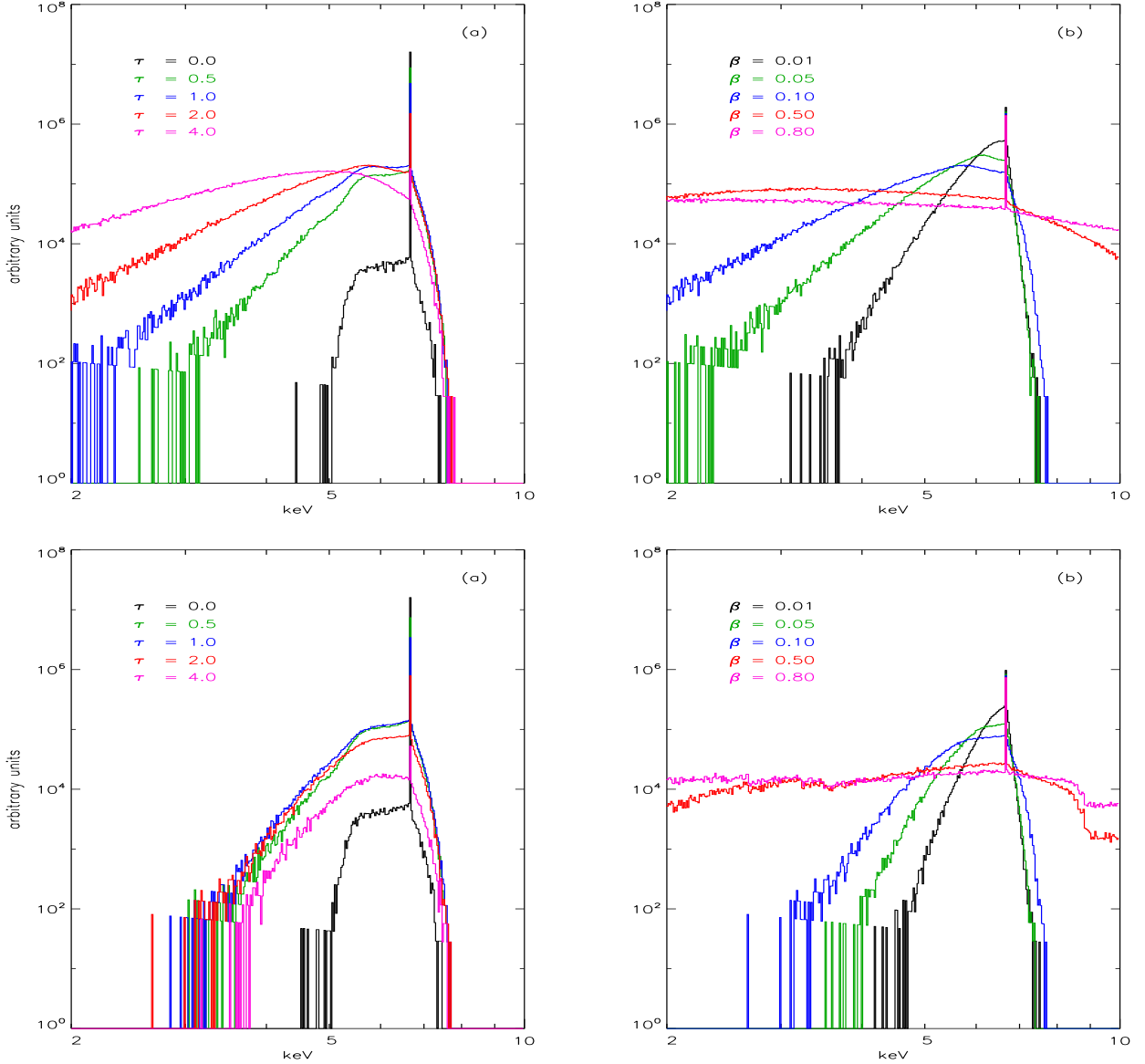


Fig. 10.— Line profiles as a function of τ and β . Primary photons are generated in the bottom of outflow. Upper panel: the line profiles for the pure scattering case. Lower panel: that for scattering plus absorption case. In each case, the fixed parameters are $E_{ph} = 6.6$ keV and $kT_e = 0.1$ keV. Spectral lines as a function of τ are for $\beta = 0.1$ and that as a function of β for $\tau = 2$. Note, the case with a notation $\tau = 0.0$ [see upper and lower panels (a)], corresponds to $\tau = 0.01$.

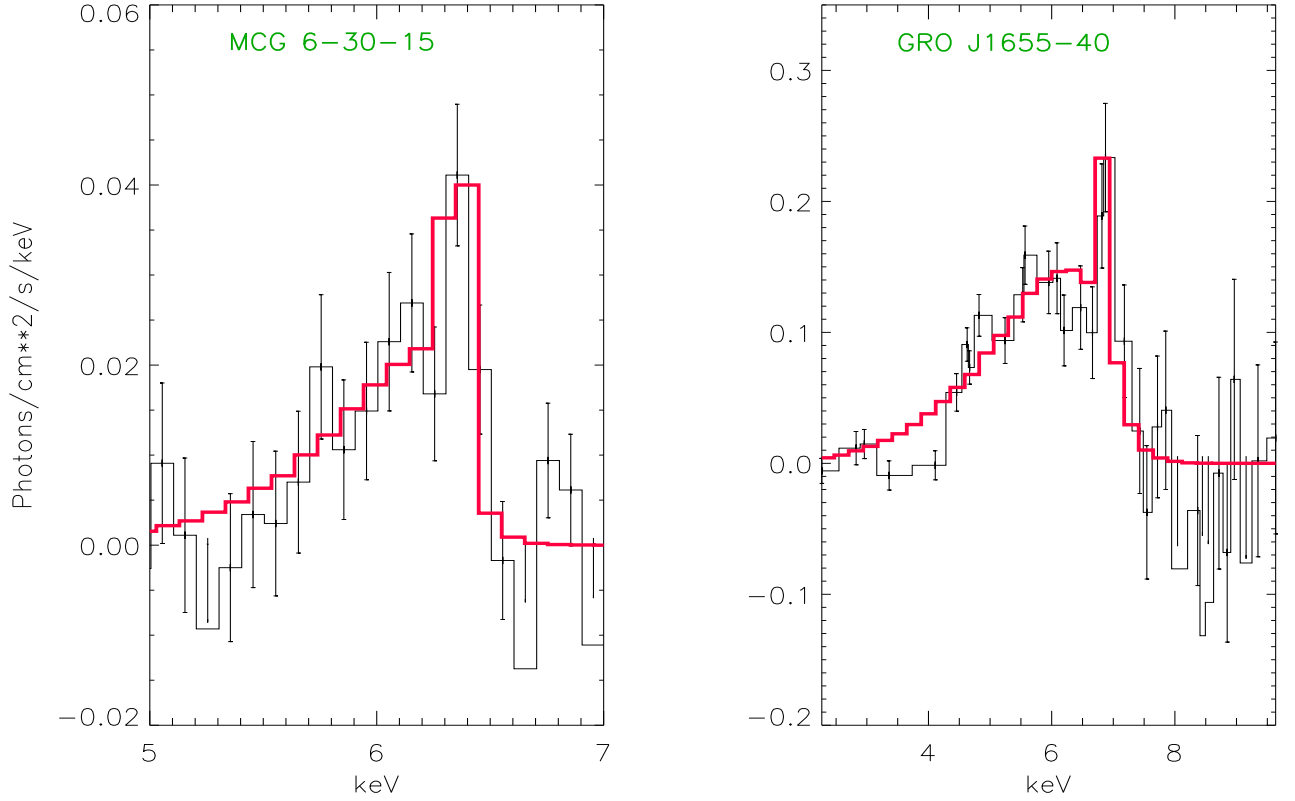


Fig. 11.— Fits of our model to the XMM observations of MCG 6-30-15 (Wilms et al. 2003) and to the ASCA observations of GRO J1655-40 (Miller et al. 2004b). For MCG 6-30-15, we have fitted the continuum with a power law of index 1.8 and compare the residuals with pure scattering model. The pure scattering model. For this model the best-fit parameters which we found are $E_{\text{ph}} = 6.51$ keV, $kT_e = 0.1$ keV, $\tau = 1.2$, $\beta = 0.02$. Primary photons are generated at the bottom of outflow (illumination of outflow from inside). For GRO J1655-40 we found the following best-fit parameters: $E_{\text{ph}} = 7.1$ keV, $kT_e = 0.1$ keV, $\tau = 2.0$, $\beta = 0.1$.

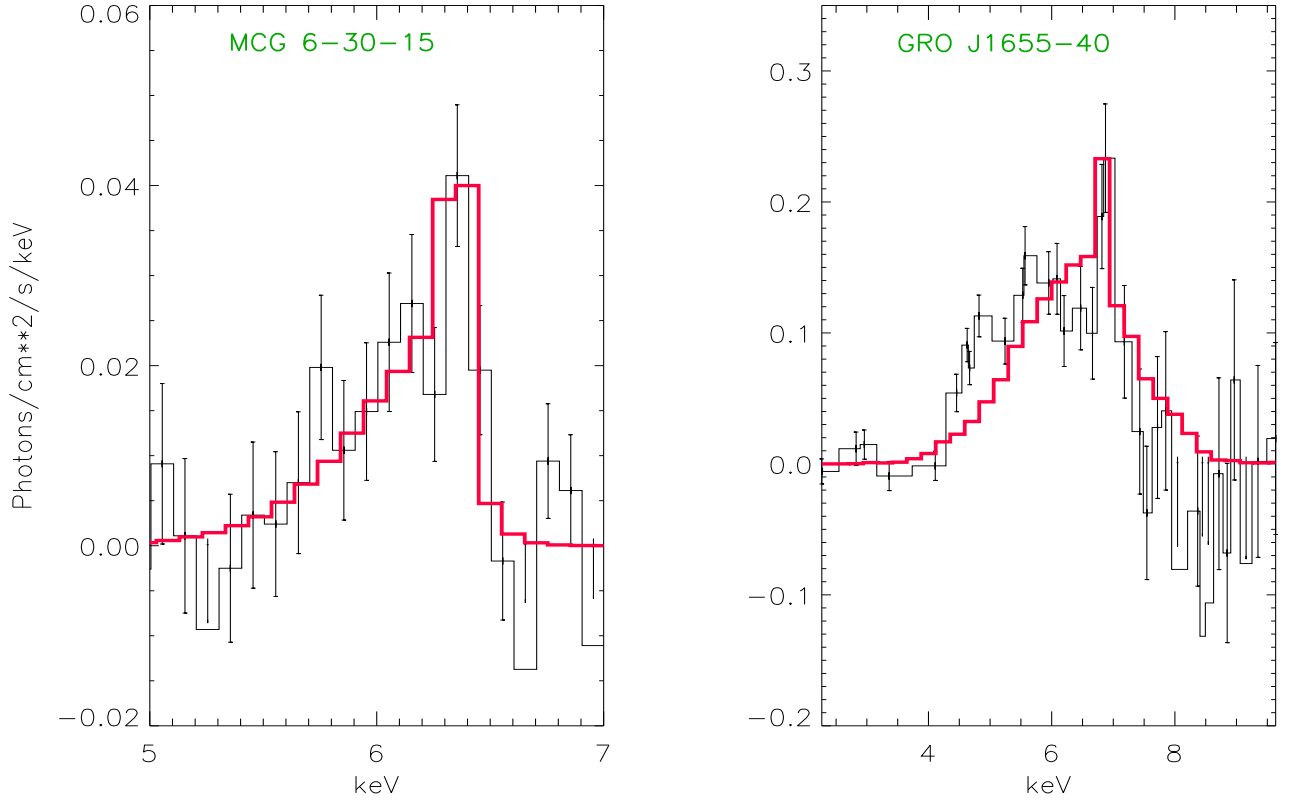


Fig. 12.— Fits of our model to the XMM observations of MCG 6-30-15 and to the ASCA observations of GRO J1655-40 using the model for which the photo-absorption along with scattering are included. For MCG 6-30-15 the best-fit model parameters which we found are $E_{\text{ph}} = 6.51$ keV, $kT_e = 0.1$ keV, $\tau = 1.7$, $\beta = 0.02$. For GRO J1655-40 we found the following best-fit parameters: $E_{\text{ph}} = 7.1$ keV, $kT_e = 0.1$ keV, $\tau = 3.3$, $\beta = 0.25$.

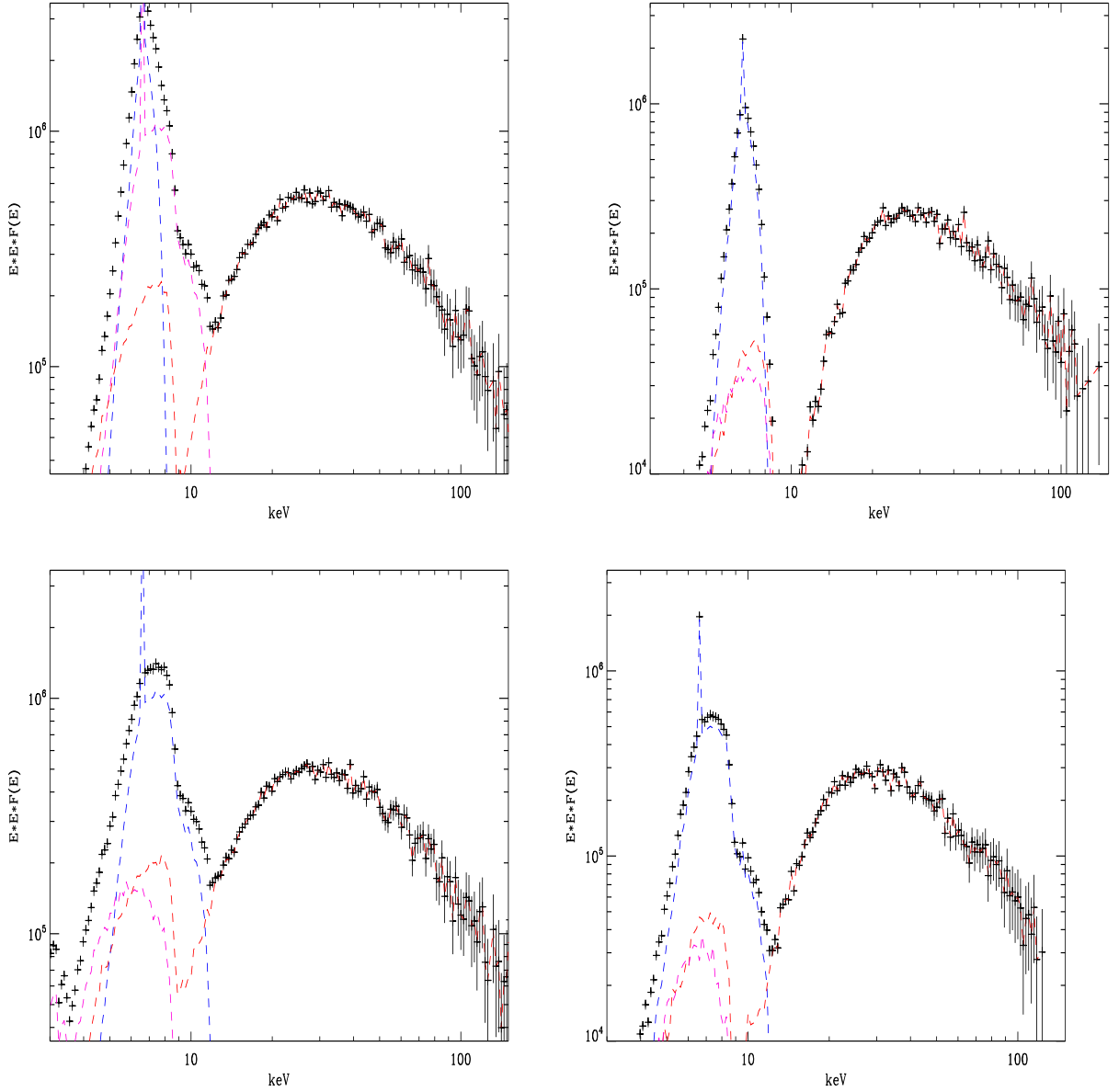


Fig. 13.— The central source spectrum reprocessed through the wind shell. Upper panel: $\beta = 0.1$ and $\tau_0 = 2$ and $\tau_0 = 4$. Lower panel: that is for $\beta = 0.3$. In the X-ray spectrum of the central source the photon numbers are the same in the blackbody and hard components. In fact, the ratio of the photon numbers is arbitrary and it depends on the illumination of the Compton cloud by the source of blackbody radiation. In this simulations we assume the blackbody color temperature is 1.2 keV. The resulting spectrum is shown by black histogram, whereas orange and pink curves present the hard and blackbody components of the central source reprocessed in the wind respectively. A blue curve is the K_α line formed in the wind. One can clearly see the strong fluorescent K_α line, K-edge formed in the wind and a prominent bump around 25 keV. The line consists of narrow and broad components (see narrow blue peak at 6.4 keV in all spectra).